Summer 8-2-2024

Mechanical Characterization of Polymer Composites Embedded with Aramid Nanofiber

Evan Griffiths

Mechanical Characterization of Polymer Composites Embedded with Aramid Nanofiber

by

Evan Griffiths

A thesis submitted in partial fulfillment of the
requirements for the degree of

M.S. General Engineering focused in Mechanical Engineering

Montana Tech

2024

Abstract

Self-healing materials are repairable and extend product lifetimes but are limited in application due to their mechanical properties such as low yield strength. Here, the mechanical properties of an elastomeric polymer composite containing aramid nanofiber are examined. These studies provided an economically feasible foundation to understand the doping concentration and resultant mechanical properties that would result should aramid nanofibers be used to reinforce a self-healing polymer that requires complex synthesis methods and expensive reactants. The elastomeric polymer used was polycaprolactone containing various weight percent aramid nanofiber. Quasi-static mechanical testing of these samples was performed following ASTM standardized tests for tension, compression, and shear. Dynamic mechanical testing of these samples was performed using a split-Hopkinson pressure bar system. The full scope of these tests provided a strong background towards the mechanical performance of polycaprolactone composite material. Similarly, a self-healing polymer was investigated that was reported to have elastomeric polymer classifications and comparable mechanical properties to polycaprolactone. Results from this work will be used to provide flexible, reinforced, self-healing composites with enhanced strength and sustainability.

Keywords: polymer, composite, mechanical properties, mechanical testing, aramid nanofiber

Dedication

I wish to thank my Mom and Dad, Amy Carter and Huw Griffiths, for their constant love and support through all the ups and downs of this research. They consistently and constantly reminded me of their pride and respect for me and my effort. Often my parents provided perspective for navigating difficult scenarios and situations with grace and patients. I cannot thank them enough for everything they have done to support me in everything I do. Similarly, I wish to thank my extended family and friends for their love and support in my efforts through their encouragement and love. Finally, I wish to thank my Grandfather, Vernon Griffiths, who was a professor at Montana Technological University and marks the beginning of my family's deep history at Montana Tech. He dedicated his life to teaching and inspired many, including me.

Acknowledgements

Research was sponsored by the Combat Capabilities Development Command Army Research Laboratory and was accomplished under Cooperative Agreement No. W911NF-15-2-0020. The views and conclusions contained in this document are those of the authors and should not be interpreted as representing the official policies, either expressed or implied, of the Army Research Laboratory or the U.S. Government. The U.S. Government is authorized to reproduce and distribute reprints for Government purposes notwithstanding any copyright notation herein. Furthermore, special thanks are given to Luke Suttey and Xavier Vorhies for their support and ideas that aided me in navigating and completing this project.

Table of Contents

List of Figures

List of Equations

Glossary of Terms

Term	Definition
polycaprolactone (PCL)	Biodegradable polyester elastomer with low melting point.
aramid nanofibers (ANF)	Para-aramid fibers with a diameter in the nanometer range.
carbon nanotubes (CNT)	Carbon tube with a diameter in the nanometer range.
cellulose nanofibers (CNF)	Wood-derived fiber with a diameter in the nanometer range.
potassium hydroxide (KOH)	In organic chemistry serves as a source of OH^- that attack polar bounds in both inorganic and organic materials.
dimethyl sulfoxide (DMSO)	Organosulfur compound that dissolves both polar and nonpolar compounds.
de-ionized water (DI water)	Water with the ions removed, increasing the purity of the water.
scanning electron microscope (SEM)	Electron microscope utilizing focused beams of electrons to scan surfaces.
diffuse reflectance infrared Fourier transform spectroscopy (DRIFTS)	Infrared spectroscopy that utilizes powder samples that collects data as a bulk sample.
thermogravimetric analysis (TGA)	Measures the thermal stability of material through thermal degradation over time.
nuclear magnetic resonance (NMR)	Instrument allowing molecular structure and composition analysis through magnetic properties of atomic nuclei.
split-Hopkinson pressure bar (SHPB)	Dynamic testing for wave propagation, compression, and dynamic flow stress and strain rate.
polytetrafluoroethylene (PTFE)	More commonly known as Teflon®, a highly nonstick and low coefficient of friction polymer.
high-speed camera (HSC)	High definition and high frame rate camera for axial compression image analysis.
infrared spectroscopy (IR Spectra)	Measurement of a samples interaction with infrared radiation to observe functional groups of materials.

1. Introduction

Self-healing materials have the potential to increase the lifetime of products exponentially through both non-reversible and reversible healing processes. The difficulty for reversible self-healing materials is their relatively poor mechanical stability; often taking the form of different classifications of polymers such as rigid plastics, flexible plastics, and elastomers [1]. The benefit to self-healing materials is their ability to repair and extend product lifetimes, but they are limited in application due to the mechanical properties. Similarly, they are difficult to study due to extensive and elaborate polymer reactions while also consisting of unique precursors that increase the const of manufacturing. Herein, it is described the use of polycaprolactone (PCL) to provide insight into polymer composite fabrication utilizing aramid nanofibers (ANF) for reinforcement [2]. The goal of this nanocomposite is to develop the mechanical understanding of polymer nanocomposites utilizing affordable methods and materials to apply towards future studies of self-healing polymer nanocomposites.

PCL is a highly sought after biodegradable and biocompatible thermoplastic with many benefits as it is commonly used within the biomedical field. The benefits for PCL as a semi crystalline polyester include high processability due to a low melting point (55-60 °C) as well as its extensive solubility in organic solvents [3], [4]. PCL’s most broad use is related to its biocompatibility where it is often used for drug delivery methods [5] as well as scaffolds for tissue engineering [6]. While PCL has incredible elongation before failure (>700 %), its tensile strength is relatively low (23 MPa) [3], [7]. PCL is used in additive manufacturing as a resin to improve end properties such as toughness, flexibility, compression and tear strength [4]. However, the addition of ANFs have the potential to create a reinforced polymer with improved strength and toughness for increased load [8], mechanical stability [9] and thermal stability [10].

Aramid fibers are made of aromatic polyamides and are synonymous with Kevlar® which are often used in ballistic applications [11]. Aramid fibers possess incredible mechanical properties, being resistant to mechanical loads in both quasi-static and dynamic applications. Aramid fiber has high performance in tensile strength and low fiber elongation [12]. These properties remain when the aramid is reduced to a nanoscale [13]. Many nanoscale materials are currently used for the fabrication and preparation of advanced composite materials. These nanoscale materials include carbon nanotubes (CNT) and cellulose nanofiber (CNF). ANFs however, are an increasingly studied material for advanced composite materials due to their incredible macroscopic performance that maintains at nanoscale levels while also exhibiting large aspect ratio and specific surface area [14], [15]. Another benefit to aramid structures is their safeness for healthy cells. A study demonstrated that aramid pulp has low toxicity over the ranges of 24, 48, and 96 hours for 3T3 cells [16]. While CNTs have been shown to be severely toxic [17] along with TiO_2 nanowires [18]. In turn, due to strong interfacial interactions [19] as well as biocompatible properties of aramid structure [7], aramid nanofibers are a strong candidate for a high performing composite material.

Increasing the mechanical stability of PCL broadens its application by making a polymer composite that is more resistant to damage and has increased durability. These improvements have the potential to create stronger structures for applications in bio-engineering applications, including but not limited to tissue engineering, bone engineering, and nerve engineering [7], [20]. For instance, PCL is commonly used in drug delivery systems as well as sutures, wound dressing, and contraceptive devices [20]. Similarly, while increasing PCL mechanical properties, it retains rheological and viscoelastic properties after ANF reinforcement [21]. In turn, PCL/ANF composite material could also be electro spun to synthesize PCL nanofibers with increased mechanical properties and advancing PCL textiles for applications in bio textiles [22]

In this work, ANFs were used to reinforce polycaprolactone to improve strength and toughness to extend the applicable uses of the polymer. Mechanical properties of the enhanced polymer were characterized in both quasi-static and dynamic testing. Quasi-static testing included standard tensile, compression and shear testing. Dynamic testing included split-Hopkinson pressure bar testing.

2. Methods

2.1. Aramid Nanofiber Synthesis

Aramid fibers possess outstanding mechanical properties due to strong and highly aligned hydrogen-bonded networks. In turn, one-dimensional aramid nanofibers, maintain the qualities of their large-scale molecular chains, but also exhibit nanoscale dimensions [23]. The fabrication of ANF was done through proton donor-assisted deprotonation of aramid fibers [14]. Aramid fibers (*0.6 g)* and potassium hydroxide (KOH) *(0.9 g)* were added to *300* mL of dimethyl sulfoxide (DMSO). De-ionized (DI) water was then added in a specific volume ratio to DMSO of 1:25 respectively. This solution was magnetically stirred for a minimum of 4 h for ANF/DMSO solution. As the solution was allowed to stir, the color of the solution transitioned from clear, to slight yellow tint, to a dark red; indicating that the hydrolysis of the aramid fiber was completed. The structural restoration of ANFs was then accomplished by utilizing DI water as a proton donor for the system. To complete the structural reconstruction of ANFs, a specific volume ratio of DI water to ANF/DMSO solution was used in a 2:1 ratio. This yielded a uniform ANF/DMSO/H_2O solution after being stirred with a magnetic stir bar for a minimum of 1 h. Further color transitions occurred that signified the completion of the structural restoration of the aramid fibers as the solutions changed from a dark red (Figure 1A), back to a slight yellow tint (Figure 1B).

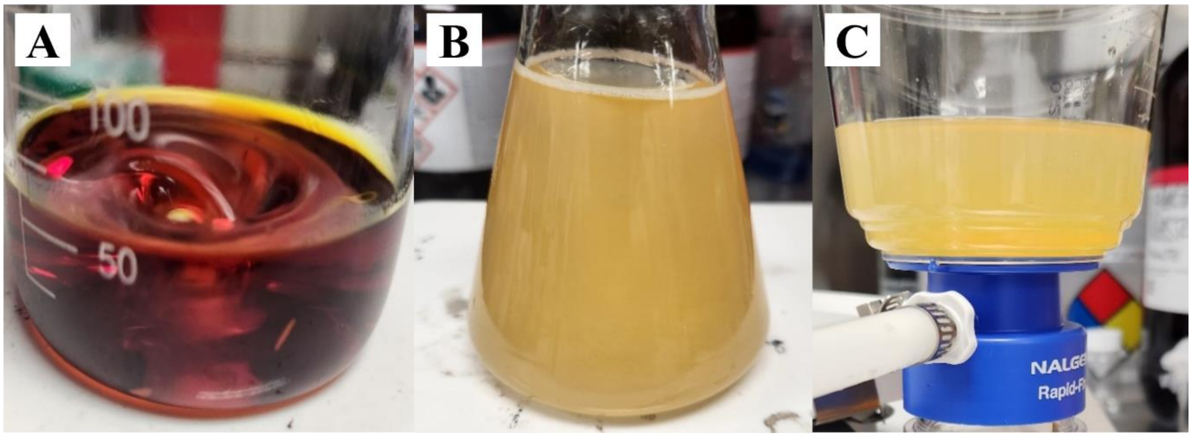

Figure 1: (A) Dissolution of aramid fibers in DMSO and KOH. (B) Reformation of ANFs upon the addition of DI water. (C) Filtration of reformed fibers through 0.2 µm filter.

To utilize the high-quality fibers formed through the reformation process, ANFs needed to be removed from the DMSO/H_2O solution and transferred to new solvents. Similarly, because the reformation process is uncontrolled, larger fibers tended to form and required the solution to be filtered. This was done by using Nalgene filter units with pore sizes of 0.2 µm and a vacuum for the filter process (Figure 1C). Next, scanning electron microscopy (SEM) using a Hitachi S-4500 and ImageJ analysis allowed for a percent area calculation to give an estimation of fibers that passed through the filter. This in turn allowed for the calculation of fibers that were retained in the filtered solution giving a concentration of ANFs within the filtered ANF/DMSO/H_2O solution.

Next, the difficulty of doping PCL with ANFs required the use of a solvent to suspend ANFs in random orientation while also ensuring even distribution within PCL. Two methods for obtaining ANFs suspended in solvents were studied. The first method utilized trifluoroethanol (TFE) for solvent transfer. This was done using dialysis tubing filled with filtered ANF/DMSO/H_2O (Figure 2A) solutions that were then suspended in a large TFE bath (Figure 2B) for a minimum of 48 hours. After the minimum 48 hours had passed, the dialysis tubing had lost a significant portion of its original volume, signifying that the DMSO/H_2O had successfully permutated through the dialysis tubing to be replaced with TFE. Similarly, the polarity difference between DMSO, Water, and TFE in the large TFE bath was observed as well as SEM micrographs of the fibers to provide further confidence that the solvent transfer had occurred.

The second methodology utilized a vacuum oven to remove DMSO and H_2O in a series of simple steps. First, the ANF/DMSO/H_2O solution was placed directly into the vacuum oven after filtration (Figure 3A). The oven was then heated to approximately 85 °C while under a vacuum of approximately 510 mmHg or greater to reduce the evaporation temperature of water. As the water evaporated from the solution, the pressure would commonly drop below the evaporation point of water. In turn, this process was monitored and consistently reperformed to aid in keeping the vacuum at appropriate levels to evaporate water. After the solution reduced in volume to approximately 50 mL (Figure 3B), indicating DMSO was the only solvent remaining in the system, the solution was transferred to a 40 mL scintillation vial in two steps of approximately 25 mL to further evaporate the remaining solution.

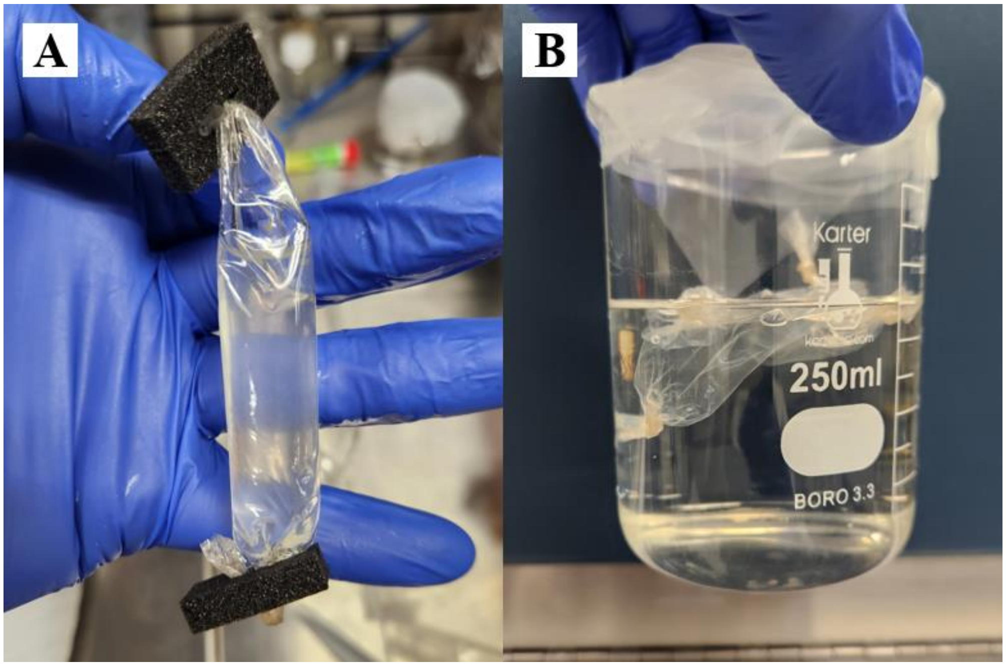

Figure 2: (A) ANF/DMSO/H_2O dialysis tubing sample, and (B) Solvent transfer through TFE bath with dialysis tubing sample.

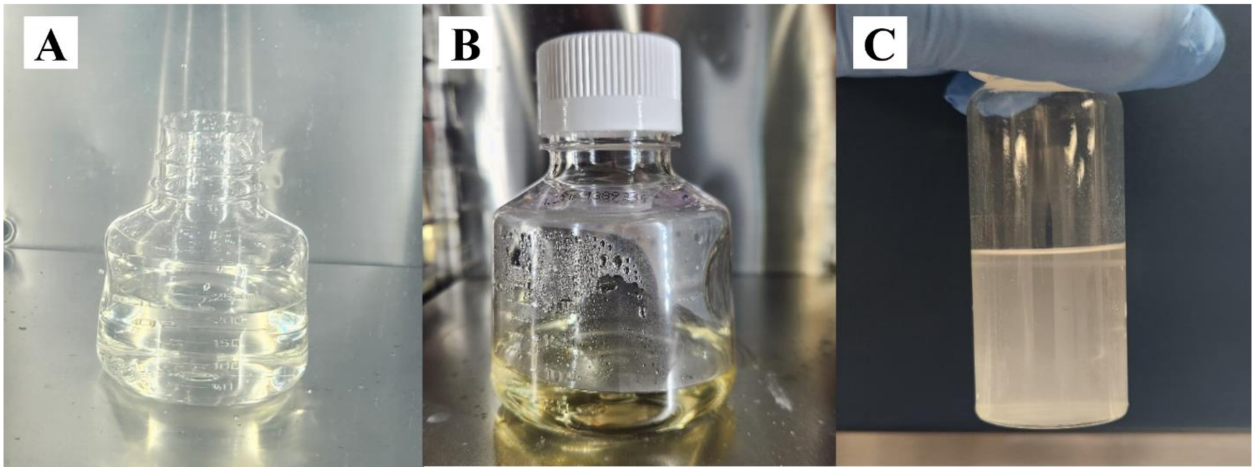

Figure 3: Volume lost over evaporation periods for ANF fabrication to resuspend ANF in TFE (A) Initial solution consisting of H_2O/DMSO/ANF. (B) Primary volume loss of H_2O to leave solution consisting of DMSO/ANF, and (C) Final product after DMSO evaporates leaving solution of TFE/ANF for polymer composite synthesis.

To evaporate the DMSO from the solution, the oven was set to 150 °C with a vacuum of 510 mmHg. If the vacuum was pulled too rapidly, or the vacuum was too high, the solution would begin to violently boil causing DMSO/ANF to boil out of the scintillation vial. In turn, vacuums were pulled slowly and carefully to retain as much ANF as possible. After the DMSO was fully evaporated from the system, a green mass would be dried to the walls of the scintillation vial which was dispersed into the required solvent TFE through ultra-sonication to obtain ANF dispersed in TFE leaving a milky white solution (Figure 3C). These solutions of ANF/TFE were analyzed through SEM (Figure 4) and ImageJ software to observe the high-quality nanofibers and concentrations of the solutions.

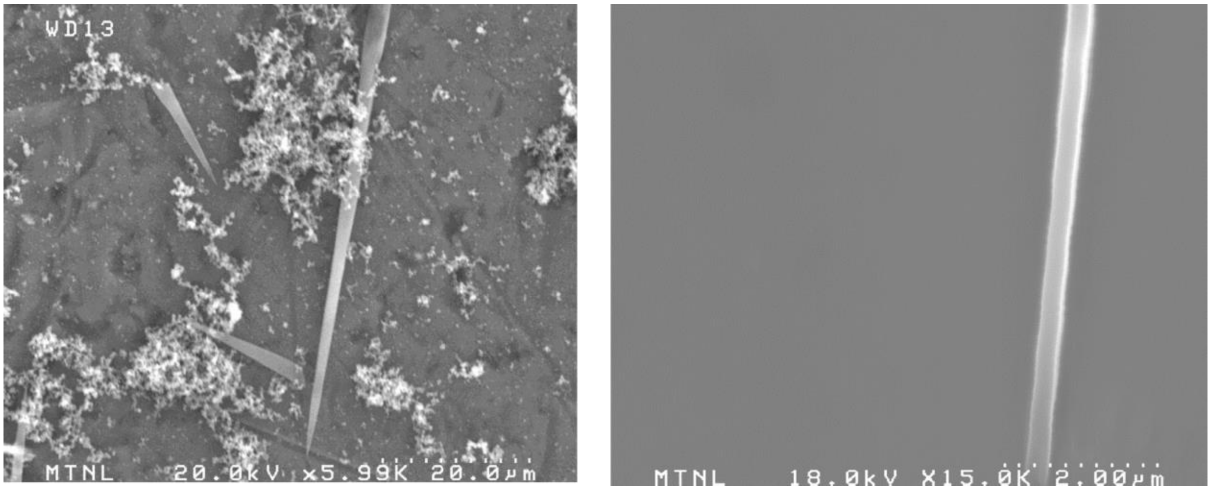

Figure 4: SEM micrographs of ANF at varying scales.

2.2. PCL Synthesis

PCL for samples and testing was synthesized from its raw form of PCL beads, by the addition of TFE to form a PCL/TFE solution at 10 weight percent PCL. The known and measured variables for forming samples of PCL were the mass of PCL and the volume of TFE. Calculations for weight percent of PCL were performed following Equation 1 to solve for the mass of TFE required for the desired weight percent of the solution. After solving for the mass of TFE required, a density conversion was performed to solve for the volume of TFE required for the solution (Equation 2) for synthesizing the desired weight percent of PCL in TFE.

$$\text{Equation 1: } m_{TFE} = \left(\frac{m_{PCL}}{wt\%_{PCL}}\right) - m_{PCL}$$

$$\text{Equation 2: } V_{TFE} = \frac{m_{TFE}}{\rho_{TFE}}$$

After forming solutions, PCL/TFE solutions were set onto a hot plate with a stir rod to dissolve PCL. PCL/TFE solutions were then redistributed using syringes and wax paper to remake PCL beads to allow excess TFE to evaporate from the newly formed sample material. Reformed PCL beads were allowed to dry for a minimum of 48 hours to ensure that excess TFE had evaporated from the system. PCL beads could then easily be taken and melted into sample molds to meet the large variety of sample shapes and dimensions required for testing. The reformation of PCL beads was important to the analysis of PCL as the synthesis of PCL/ANF required being dissolved by TFE. To fully analyze the effects of ANF of PCL, the PCL was dissolved in TFE for solvent effect quantification.

2.3. Preparation of Self-Healing Polymer

2.3.1. Monomer Synthesis

Preparation of monomer was performed following predetermined methodology for polymer noted as P6 [1]. P6 utilized anisylpropylene with a methyl subgroup notated as $A^{Me}P$. For preparation of $A^{Me}P$, magnesium turnings (*3.3 g*), anhydrous lithium chloride (*5.3 g*), a catalytic amount of iodine (*0.05 g*), and *300* mL of anhydrous tetrahydrofuran were added to a *500* mL three-neck flask in an argon atmosphere creating a clear orange solution. Magnesium turnings, lithium chloride, and glassware were kept in an oven overnight to remove excess water that could inhibit the reaction. Prior to introducing chemicals into the dried glassware, argon gas was backfilled into the three-neck flask to provide an inert atmosphere for the reaction. After forming the initial step of the reaction (Figure 5A), the reaction mixture was heated to reflux (approximately 66 °C) and 2-bromo-4-methylanisole (*25.0 g*) was added dropwise, causing the solution to turn cloudy white (Figure 5B), signifying critical addition of 2-bromo-4-methylanisole. This solution stirred for 1 hour at room temperature and turned a dark green color (Figure 5C), as the magnesium turnings reacted to form the corresponding Grignard reaction, where allyl bromide (*22.6 g*) was then added slowly. This reaction mixture stirred overnight and quenched the next day with saturated ammonium chloride aqueous solution causing the solution to turn light green (Figure 5D). After quenching the product and allowing the mixture to stand, the organic layer separated in the solution (Figure 5E).

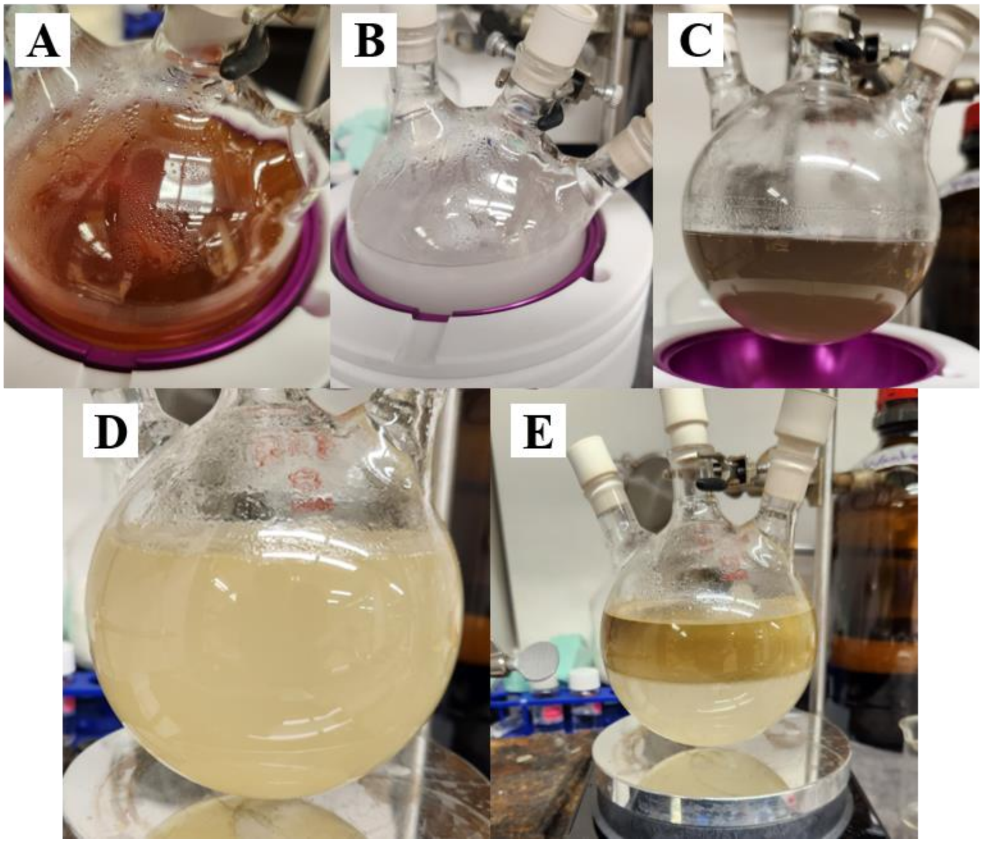

Figure 5: (A) First step of monomer reaction with magnesium turnings, lithium chloride, iodine and tetrahydrofuran. (B) Second step of monomer after 2-bromo-4-methylanisol dropwise addition. (C) Third step of monomer reaction showing magnesium turnings integration. (D) Fourth step of monomer reaction after quenching solution with saturated ammonium chloride aqueous solution. (E) Final step of monomer reaction showing organic layer separation.

After performing the base reaction $A^{Me}P$, as a crude product, required purification. This was performed through rotary evaporation to remove excess tetrahydrofuran after harvesting the organic layer via separatory funnel. This product was then purified by column chromatograph over silica gel, utilizing n-hexane to separate the analyte $A^{Me}P$ from reaction mixture. The product obtained from liquid chromatography columns was collected in small beakers to track product progress through the column using thin layer chromatography plates. An example of the silica gel chromatography column and the thin layer chromatography plate tracking are shown in Figure 6

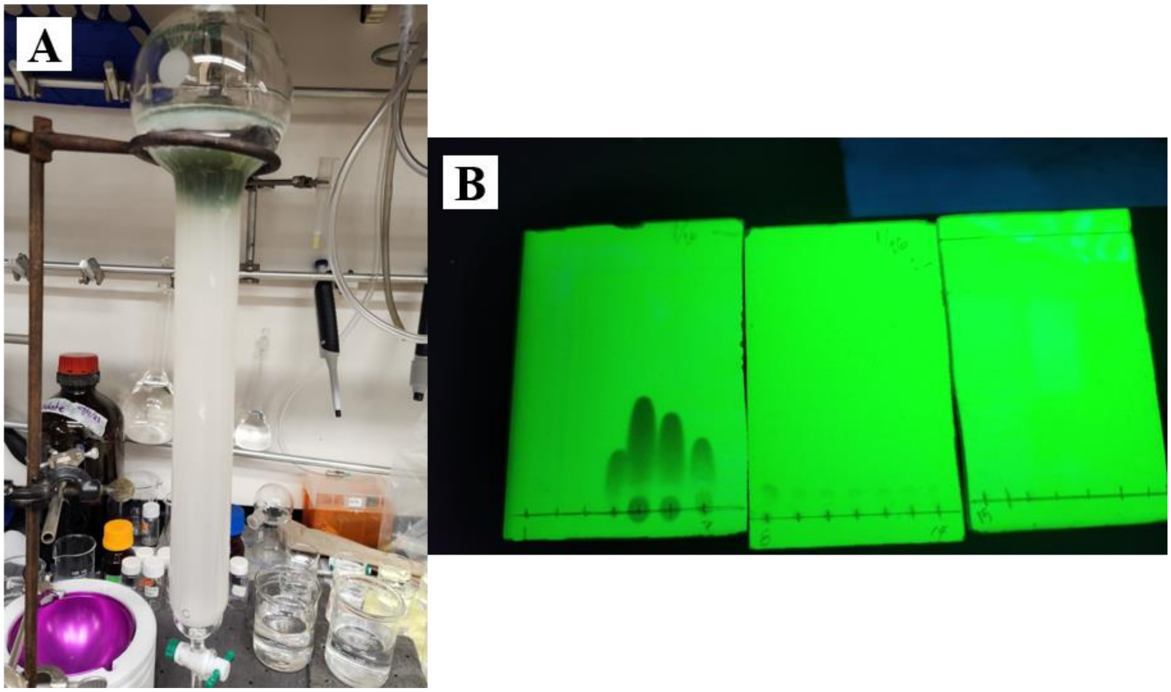

Figure 6: (A) Silica gel chromatography column using n-hexane to separate $A^{Me}P$ as precursor for polymer reaction. (B) Thin layer chromatography plates for tracking $A^{Me}P$ progress through the column.

Thin layer chromatography plates (Figure 6B) were critical for tracking $A^{Me}P$ as it passed through the column. All product that was filtered through the column appeared colorless as it transferred into the small beakers as shown in the bottom of Figure 6A. In turn, every tick mark on the TLC plates represents a beaker containing filtered solution. While only the lines traveling up the TLC plates shows an individual beaker containing portions of $A^{Me}P$. As seen in Figure 6B, some lines were much more prominent and traveled much further than others. This suggests that some side reactions occurred as the molecules have molecular weight differences based on their travel distance on the plates, resulting from interactions with the silica of the plate. Similarly, other beakers had no $A^{Me}P$ present after passing through the column. This method allowed for easy and convenient tracking of $A^{Me}P$ through the column. After the product was fully collected, rotary evaporation was used to remove n-hexane from the product, for use in the self-healing polymer reaction.

2.3.2. Polymer Synthesis

Polymer synthesis was attempted following previous work [1]. While performing this work, it was critical that it was performed in an inert atmosphere. This was done using a glovebox with nitrogen atmosphere to handle all chemicals. A toluene solution (*2* mL) of $(C_5Me_4SiMe_3)Sc(CH_2C_6H_4NMe_2\text{-}o)_2$ (catalyst) (*5.1* mg) and $[Ph_3C][B(C_6F_5)_4]$ (radical initiator) (*9.2* mg) was prepared in scintillation vials in the inert atmosphere of the glovebox. Similarly, a toluene solution (*150* mL) of $A^{Me}P$ (*740* mg) was prepared and charged into a three-necked flask with a magnetic stir bar. The three-necked flask was then set in a water bath and connected to a well-purged Schlenk ethylene line. Ethylene was bubbled into the system, saturating the solution by stirring for a minimum of 2 minutes. Here, the prepared scintillation vials of catalyst and radical initiator was added through a syringe under vigorous stirring for 5 minutes. After stirring, the polymerization quench was attempted by adding methanol (*150* mL) to the solution. Unfortunately, for our synthesis, no polymerization was observed in any attempts. Further attempts yielded the same results after attempting with excess catalyst and radical initiator in the following attempts. Figure 7 depicts attempts taken with excess catalyst and radical initiator masses.

Figure 7: Individual polymerization attempts utilizing excess catalyst and radical initiator in attempt to propagate and excite reaction for polymerization reaction. Color difference indicate changes in exceeding amounts of catalyst and radical initiator.

When re-attempting the polymer synthesis process, several different factors were considered in the attempt to quench the product. The first factor that was considered was increasing the catalyst and radical initiator amounts to ensure the reaction had the chemicals in excess to produce any potential products. The second factor considered was the batch of monomer used. When preparing for the polymerization reaction, several batches of monomer were prepared to expedite the polymer reaction. Each monomer batch likely had varying purity levels within reason. In turn, each monomer batch was also tested in the attempt to produce a polymer quench.

2.4. PCL Aramid Nanofiber Composite Synthesis

PCL/ANF composite synthesis was completed using TFE doped with ANFs. A critical aspect to the synthesis of PCL/ANF composites was introduction of irregular agitation to randomly disperse and orient ANFs within the PCL matrix. This incurred the use of a sonication bath to easily and reliably manipulate ANF/TFE solution. While ANF/TFE solution was being sonicated, PCL was also introduced into the system to create PCL/TFE/ANF solutions at varying ANF concentrations. In order to accurately dope PCL samples with ANF, weight percent methodology from Equation 1 was adapted into Equation 4 for weight percent ANF in PCL. Equation 4 considers the mass of ANF present in ANF/TFE solution (Equation 3) to define the mass of PCL required. Equation 1 is used solve for the volume of TFE required based on the mass of PCL required by Equation 4. Sample synthesis uses ANF as a limiting factor and setting desired ANF weight percent.

$$\text{Equation 3: } m_{ANF} = \frac{C_{ANF/TFE}}{V_{ANF/TFE}}$$

$$\text{Equation 4: } m_{PCL} = \left(\frac{m_{ANF}}{wt\%_{ANF}}\right) - m_{ANF}$$

Concentration of ANF/TFE solution was based on the volume of TFE present in the ANF/TFE solution, volume of solution placed onto SEM stub for ImageJ analysis, and area percent of the fibers on the stub calculated through ImageJ thresholding analysis (Figure 8). After PCL is introduced into the ANF/TFE solution, heating the sonication bath increased the fluidic state of the system, which was aided by the low melting point of PCL. These solutions were allowed to sonicate for a minimum of 15 minutes to ensure randomized orientation of ANFs.

After sonication was completed, PCL/TFE/ANF beads were formed onto wax paper to allow TFE to evaporate from the samples to form PCL/ANF composite beads. These beads were easily manipulated and melted into different sample molds to meet sample size and dimension requirements for mechanical testing of PCL/ANF composites. The weight percent of ANF in PCL was then calculated through the knowledge of ANF/TFE concentration previously described and mass of PCL. This allowed for the analysis of PCL at 1 wt% and 2 wt% ANF. Weight percent of ANF was chosen based on the previous studies that utilize ANF composites that exhibited desired mechanical properties [16], [19], [24], [25]. To fully characterize ANF effects on mechanical performance, solvent dissolved PCL was also considered during testing to provide a more complete scope of PCL mechanical properties and its reactions after solvent dissolved and ANF impacts.

2.5. Characterization

2.5.1. ANF Characterization

SEM was used to observe successful formation of fibers after hydrolysis and to calculate area percentage for ANF/TFE concentrations. After several micrographs were obtained to represent the ANF sample, ImageJ was used to calculate the area covered by fibers throughout all the micrographs captured. ImageJ calculated area covered through thresholding the contrast of the picture by approximately 5 %, then counting the highlighted pixels (Figure 8B). This

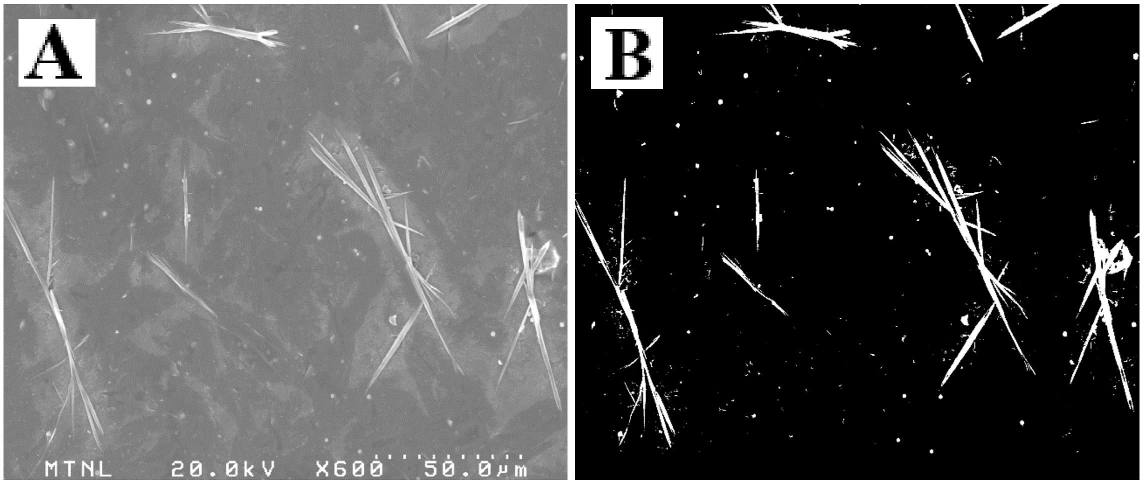

Figure 8: (A) SEM Micrograph of ANF after sonication in TFE to estimate volume fractions of fibers present in solution, and (B) ImageJ analysis of SEM shown in A.

supplied an average area percent of fibers to convert to a volume percent for the sample volume. For this calculation volume of the solution, density of the Kevlar® and density of TFE were used to calculate a concentration of the solution. An example of the imaging for this process is shown in Figure 8.

A minimum of eight micrographs were obtained to estimate the concentration of the sample volume. Some error is expected when performing contrast threshold manipulation of micrographs. This often occurred in small particles being present. This error is mitigated by manually reducing the threshold as much as possible to include as much fiber as possible while reducing external factors that would increase the area fraction. These external factors include small, highlighted particles that did not show distinct fiber morphology. However, due to the fiber size distribution, it cannot be fully concluded these particles were not incredibly small ANFs.

ANFs were analyzed utilizing diffuse reflectance infrared Fourier transform spectroscopy (DRIFTS) to obtain infrared spectra (IR spectra) of fibers after reformation. IR spectra aided in concluding that the product of ANF chemically matched macro scale fibers. This corresponds to the mechanical performance of ANFs maintaining the robust properties of the classic aramid fibers. Comparing the ANF DRIFTS spectra to macro scale aramid fiber spectra shows matching transmittance/absorbance peaks shown in Figure 9.

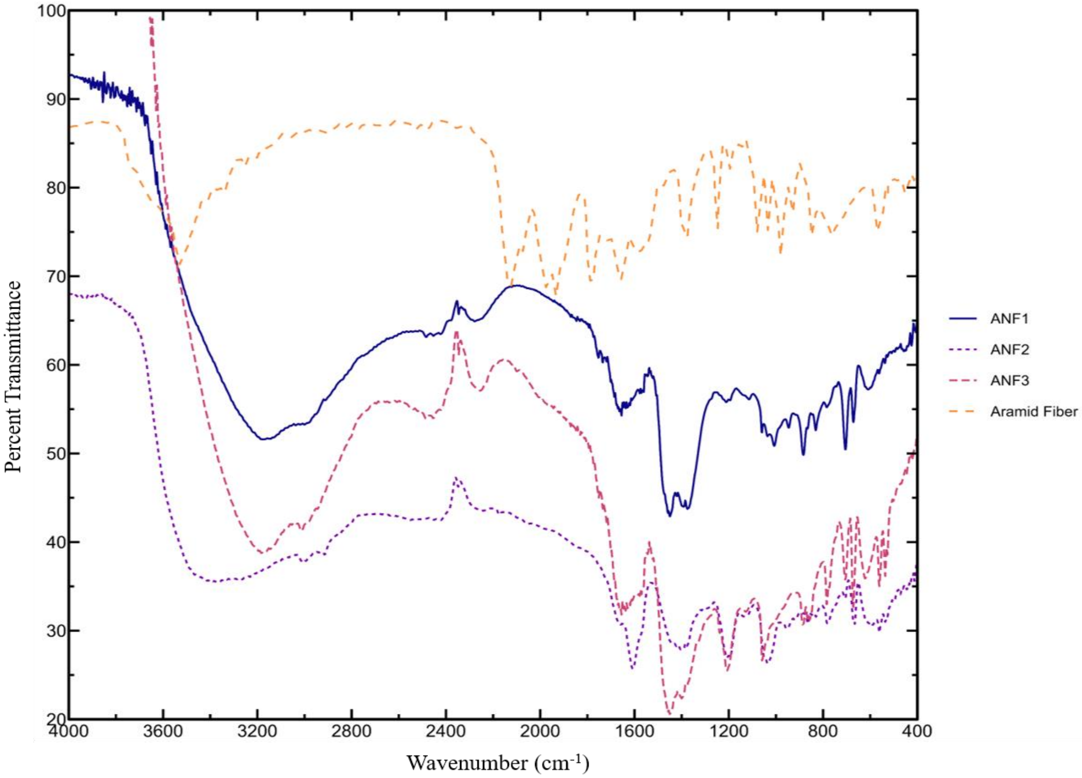

Figure 9: DRIFTS of ANF collected via IRTracer-100 and aramid fiber spectra**.**

Key peaks that define the functional properties of aramid fibers are located at approximately 3300 cm^{-1} which defines NH stretching vibrations, 1510 cm^{-1} for C-C stretching vibrations of the aromatic ring, and 1246 cm^{-1} and 823 cm^{-1} for the out-of-plane vibrations of the phenyl group [16], [26]. Matching peaks for the transmittance properties can be confirmed through the comparison of the aramid fiber versus ANF lines. This gives confidence moving forward that the process of ANF synthesis is reliable and repeatable for polymer composite development and reinforcement. Similarly, the functionality of ANF at nanoscales remains consistent based on the matching functional groups. This in turn allowed for the continuance of the characterization of native PCL, solvent dissolved PCL, and PCL with one and two weight percent ANF through thermogravimetric analysis (TGA). TGA allows for the classification of thermal property characterization and the effects of solvent on polymer as well as the doping of ANF within the PCL matrix (Figure 10).

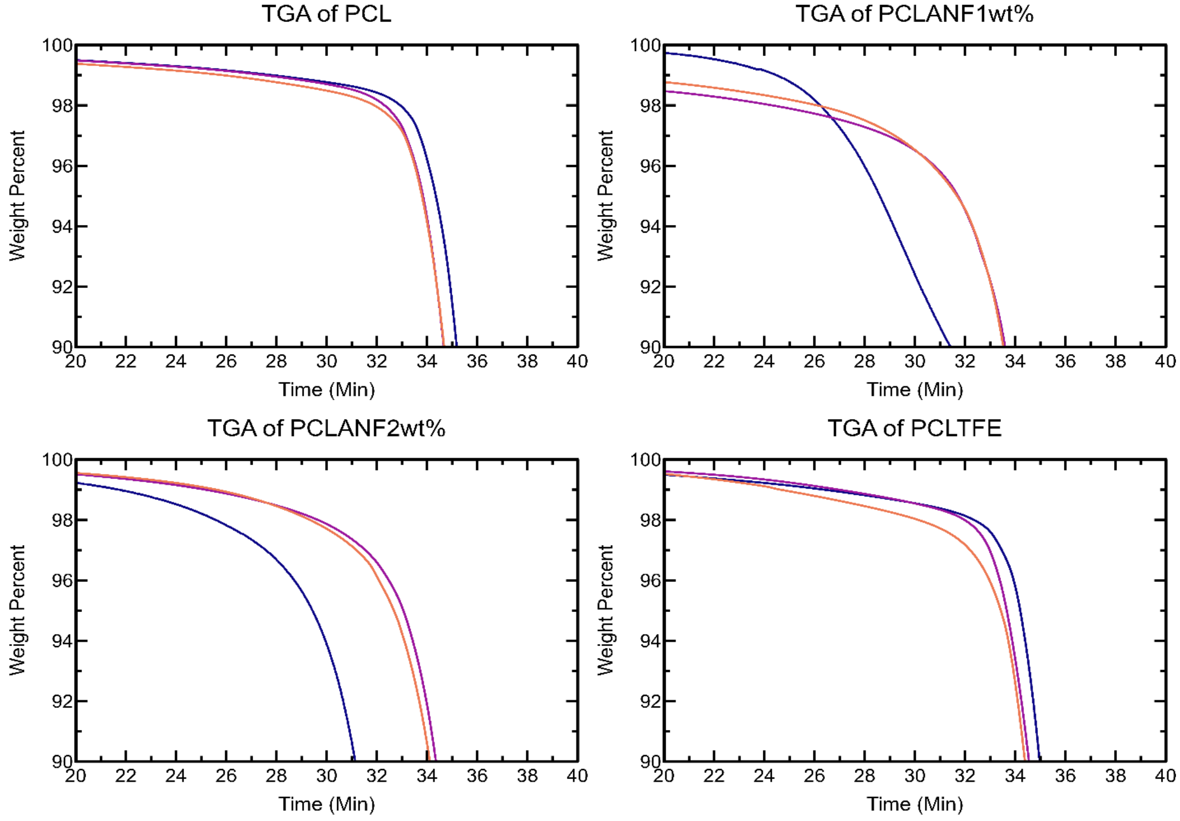

Figure 10: TGA for the complete range of PCL samples.

TGA for the complete set of PCL sample yielded that there was a singular onset decomposition point throughout the sample set. This concludes that ANF did not induce secondary onset points and that TFE has fully evaporated from the samples. In turn, the major conclusion drawn from this analysis was that TFE as a solvent slightly degraded the thermal stability of PCL after being dissolved, minorly decreasing the onset temperature. This likely occurred due to a loss in crystallinity after PCL was dissolved in TFE. In turn, degradation curves became more inconsistent after the samples had been dissolved and precipitated. ANF doping may have slightly aided in samples thermal resistance slightly increasing the onset point compared to PCL/TFE. However, this cannot be strongly concluded and should be re-analyzed at greater ANF weight percent.

2.5.2. Monomer Characterization

Proton and carbon nuclear magnetic resonance (NMR) was used to characterize and validate the process of monomer fabrication techniques. NMR data collected was compared directly to NMR data collected by original work [1]. When comparing proton NMR data, key peaks exist at approximately 4 ppm and 2 ppm with other minor peaks at 6 ppm and 5 ppm. Overall, the comparison signified that the two chemicals had similar structures, with some minor impurities present signified by peak intensity and peak quantities. Similar conclusions were made for carbon NMR data key group appear at approximately 130 ppm with several minor peaks present in the 60 ppm to 15 ppm range. Comparing the carbon NMR yields more significantly that the monomer synthesized is less pure than the original work. This is shown by the numerous smaller peaks present throughout the major comparison bonds. The proton and carbon NMR data comparing to the original data is shown in Figure 11.

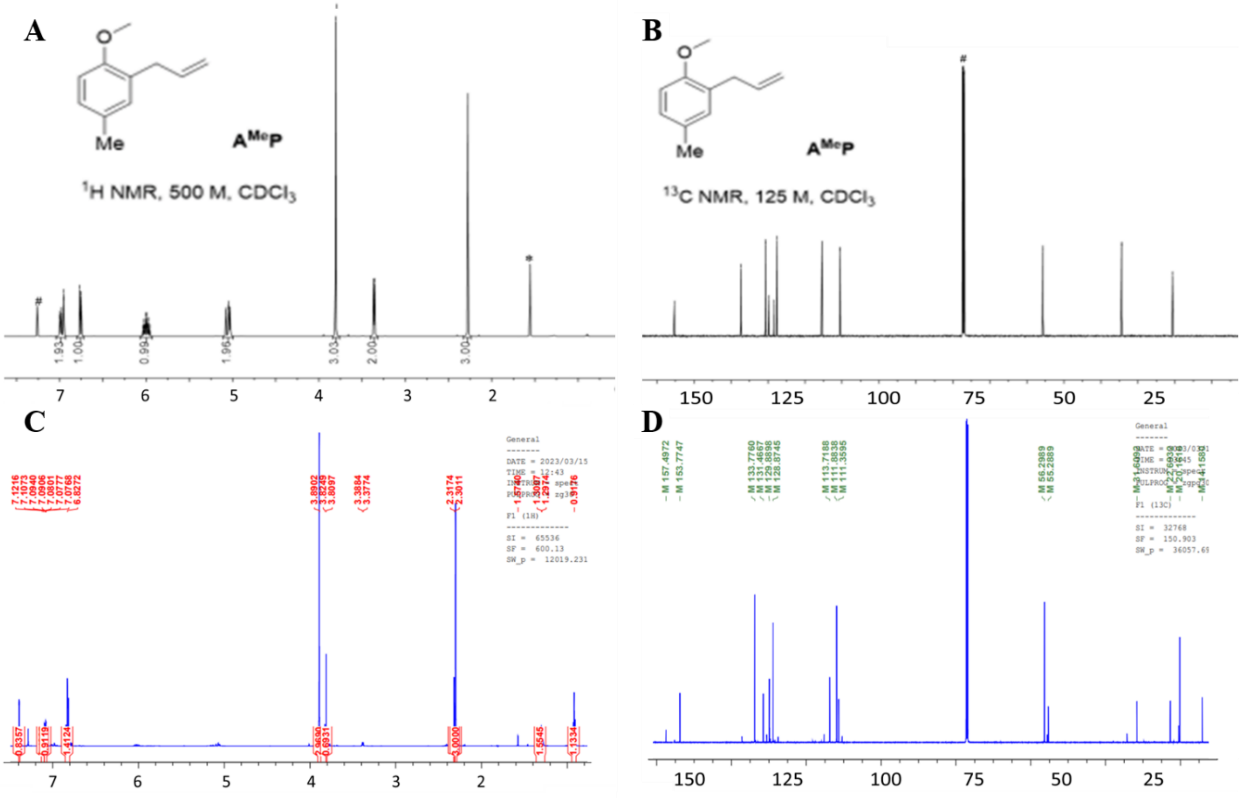

Figure 11: (A) Proton NMR adapted from Wang et al 2019 of A^{Me}P. (B) Carbon NMR adapted from Wang et al 2019 of A^{Me}P, and (C) Proton NMR of A^{Me}P, and (D) Carbon NMR of A^{Me}P.

Peaks that show the impurities of the product the likely impurities of the monomer for proton NMR are highlighted at 6 ppm, 5 ppm, and 1 ppm. Most significantly, the peaks at 6 ppm and 5 ppm are much less intense and in turn, show varying peak quantities compared to original work. Furthermore, the peak at 1 ppm is much more intense, where original work shows minimal intensity. Similarly, impurities of the product are shown in the carbon NMR most blatantly in the 25 ppm range. Original work shows two separate, singular peaks where synthesized product displays erratic and numerous peaks within the 25 ppm range. This behavior is shown again at approximately 110 ppm, where erratic peaks are displayed for the synthesized product. This overall behavior and comparison show that the synthesized product has similar structure but lacks the lab grade purity likely produced in the original work.

2.6. Mechanical Properties Testing

Tensile testing of PCL and PCL/ANF composites was performed to observe the elastic modulus changes in PCL compared to PCL/ANF composites with increasing ANF weight percent. Tensile testing was an important test to consider in order to fully characterize the material and how the materials properties were manipulated up the addition of ANF reinforcements. Similarly, compressive testing was also performed to characterize PCL and PCL/ANF in compression. This test was also important as in provided background information to split-Hopkinson pressure bar (SHPB) testing by allowing for the observation of quasi-static compressive yield strength and compressive young's modulus. The final quasi-static test performed was shear testing of the PCL and PCL/ANF composites. Shear testing provides more in-depth information to the interaction between the PCL matrix and the ANF reinforcement. While shear testing to gather data on the shear modulus of the material was important, it also allows for the development of understanding the interfacial interactions between the fibers and their propensity to adhere to the matrix in such a manner that will increase the strength of the PCL. Prior to performing quasi-static loading tests on PCL, it was important to observe the mechanical effect of TFE dissolving PCL. This would in turn provide background information on the base line PCL material and allow for further comparison after the ANF reinforcement.

2.6.1. Tensile Testing

Tensile testing was conducted to characterize PCL and PCL/ANF composites under tensile loading following ASTM D638-02A with test frame MTS Criterion Model 41, 250N loadcell at a test rates of 4 mm/min and 240 mm/min [27]. The purpose of tensile testing was to obtain and observe the properties of PCL when placed in tension to compare these results to solvent dissolved PCL as well as the reinforced PCL at both one and two-weight percent ANF.

Similarly, the two testing rates provide further information to the performance of the polymer by reducing the flow orientation exhibited by the polymer. This allows for a more specific analysis of the ANF reinforcement by reducing elongation potential. These characteristics were important for observation as they allow for characterization in the alignment of ANF fibers within the matrix when compared to other moduli changes, while also allowing for the observation of the general improvement of the material with ANF reinforcement. The calculation for engineering stress and engineering strain are given in Equation 5 and Equation 6 respectively.

$$\text{Equation 5: } Engineering\ Stress = \frac{Tensile\ Load}{Cross\ Sectional\ Area} = \sigma_{eng}$$

$$\text{Equation 6: } Engineering\ Strain = \frac{L - L_0}{L_0} = \varepsilon_{eng}$$

Engineering stress and engineering strain describe the stress and strain a sample experiences prior to any deformation. In turn, engineering stress and engineering strain assume minimal deformation within the samples. Engineering stress and engineering strain are relevant forms of stress and strain for samples that have minimal deformation. However, due to the inherent mechanical deformation properties of PCL, true stress and true strain were required. True stress and true strain equations are shown in Equation 7 and Equation 8.

$$\text{Equation 7: } True\ Stress = \sigma_{eng} * \left(1 + \varepsilon_{eng}\right) = \sigma_{true}$$

$$\text{Equation 8: } True\ Strain = \ln(\,1 + \varepsilon_{eng}) = \varepsilon_{true}$$

True stress and true strain consider the deformation of the sample into the calculation based on the engineering stress and engineering strain values. Due to the incredible elastic property of PCL, true stress and true strain calculations were used for analysis. In turn, for the tensile properties, high peaks of ultimate stress can be expected as the sample decreases in cross-sectional area over the test. Similarly, this relationship was further explored through the implementation of two different crosshead speeds. Samples were tested in sets of five and were dimensioned pre and post testing.

2.6.2. Tensile Testing Sample Preparation

Tensile testing samples were prepared by utilizing a 3-D printed 30 mm square as well as a polytetrafluoroethylene (PTFE) film to ensure easy release from the sample mold. PCL beads and PCL/ANF beads were heated to approximately 90 °C to ensure PCL would be adequately heated to its melting point while also removing as many air gaps as possible to prevent voids from forming within the sample. As the sample reached uniform heat levels, the sample was also compressed using a vulcanizer to further reduce the possibility of voids and increase uniformity of the sample. After full compression of the PCL layer, more PCL would be added and heated until an adequate height was achieved based on the dimensions required for ASTM D638-02A dog bone samples. Once the square PCL sample was sufficiently cooled, the sample could then be cut to dog bone shape using the "Print-a-Punch" developed by Boise State University [28] (Figure 12).

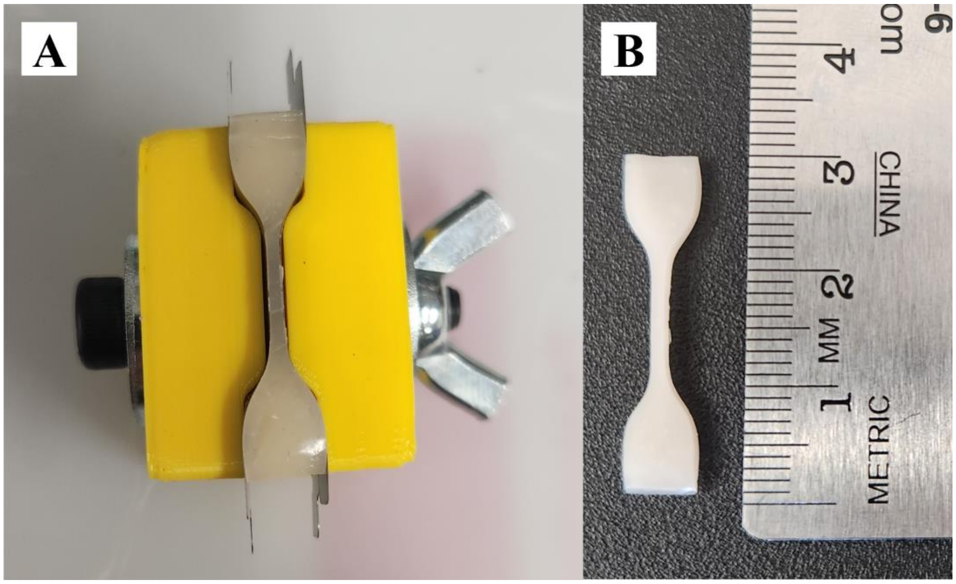

Figure 12: (A) PCL dog bone cut from PCL sheet using Print-a-Punch, and (B) PCL dog bone next to ruler for scale.

Samples sets were made in groups of five. To fully define the dimensions of the sample, the gage area was measured in three separate areas to measure uniformity and provide cross-sectional area for failure analysis of the sample. The sample was also measured for length for elongation calculations prior to testing.

2.6.3. Compression Testing

Compression testing was performed on PCL and PCL/ANF composites following ASTM D695 [29] with test frame AGS-X, 50kN Shimadzu at a testing speed of 1mm/min. The purpose of this testing was to obtain and observe the properties of native PCL under quasi-static loading to obtain compressive young's modulus and compressive yield strength for comparison to solvent dissolved PCL as well as the reinforced PCL at both one and two-weight percent ANF. In order to characterize the compressive modulus for the complete range of PCL samples, an adaptation to Equation 7 and Equation 8 is required shown by Equation 9 and Equation 10.

$$\text{Equation 9: } True\ Stress = \sigma_{eng} * \left(1 - \varepsilon_{eng}\right) = \sigma_{true}$$

$$\text{Equation 10: } True\ Strain = -\ln\left(1 - \varepsilon_{eng}\right) = \varepsilon_{true}$$

The modification to Equation 7 and Equation 8 comes in the form of distinct and key minus signs that compensate for the direction of the test. Where the tensile testing causing necking the samples and a decrease in sample cross-sectional area, compression testing creates bulging in samples and an increase in cross-sectional area. Similar to tensile testing, PCL has considerable compressive properties and is highly ductile. This allows for large sample changes when experiencing load. In turn, utilizing Equation 9 and Equation 10 accounts for the compressive sample deformation pattern commonly experienced. Samples were tested in sets of five and dimensions were recorded pre and post compression.

2.6.4. Compression Testing Sample Preparation

Compression testing samples were prepared by utilizing copper tubing as a pre-dimensioned mold to ensure radius specificity. A hot plate was heated to approximately 90 ˚C to ensure PCL and PCL/ANF would be adequately heated to achieve melting and remove potential air gaps. Samples were also compressed by hand using rods that fit within the copper tube to ensure compaction as well as sample uniformity. When sample volume surpassed the volume of the mold, a vulcanizer was used to fully compress the sample into the mold with approximately 400 psi. This compression aided in sample uniformity and face-to-face alignment. The benefit of using copper tubing as a mold was copper's inherent heat conductivity allowed for a more thermally stable heating process, such that heat was more evenly applied to the entire sample as they were heated. Samples were also placed on PTFE film to ensure easy release from the hotplate surface. To begin sample molding, a thin layer of PCL or PCL/ANF beads was inserted into the copper tubing and allowed to melt. Next, the sample would be compressed to ensure uniformity within the sample while also removing airgaps that could be present. This process would be repeated several times until the final compression using the vulcanizer where the sample would then be removed and allowed to cool to its final dimensions. After cooling, the PCL and PCL/ANF composites were easily released from the copper tubing mold (Figure 13).

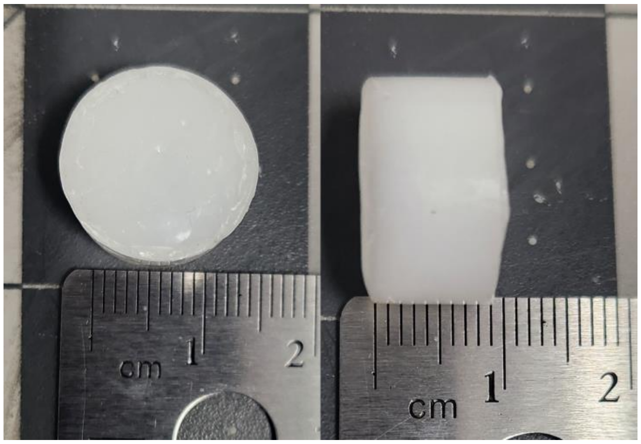

Figure 13: PCL compression testing samples.

2.6.5. Shear Testing

Shear testing was performed in accordance with ASTM D732-17 (Figure 14) utilizing test frame AGS-X, 50kN Shimadzu at a testing speed of 1.27mm/min [30]. The diameter of the punch used was 50.75 mm. The purpose of this testing was to obtain and observe the properties of PCL under quasi-static loading to obtain shear strength PCL for comparison to solvent dissolved PCL as well as the reinforced PCL at both one and two-weight percent ANF. Samples were tested in sets of six where the thickness of the samples were recorded prior to testing.

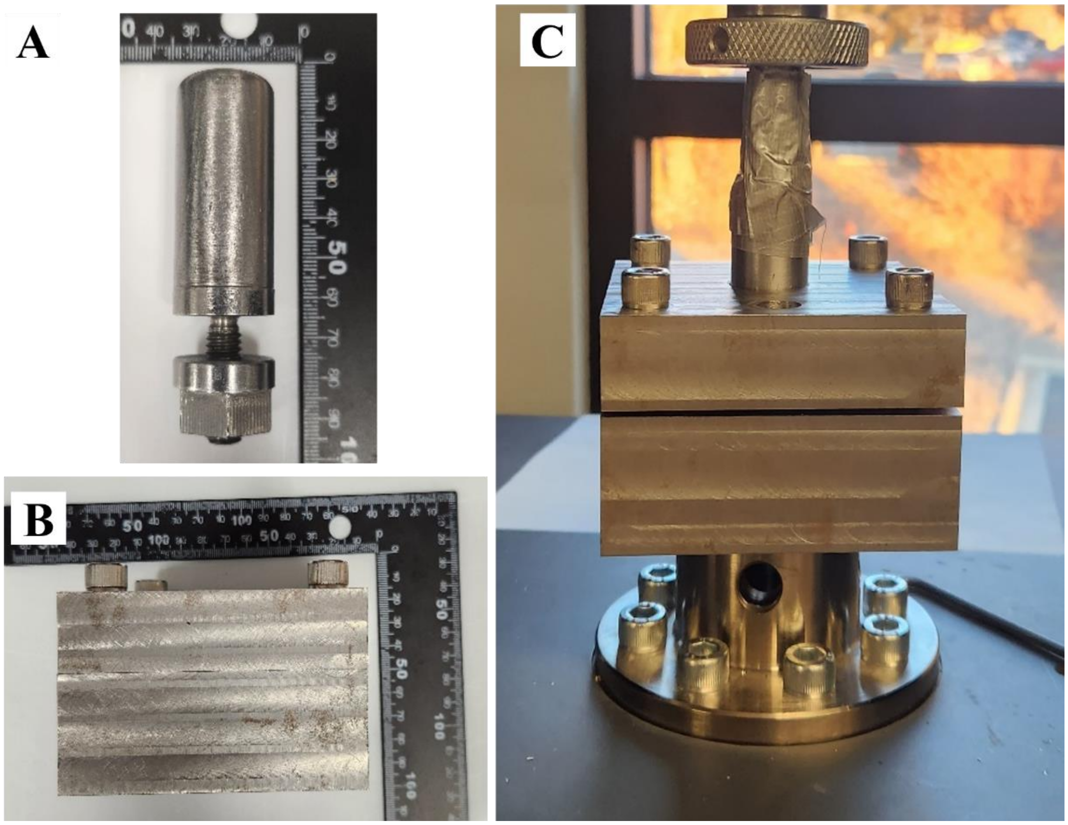

Figure 14: (A) Shear pin (B) Steel block for clamping samples, and (C) ASTM D732-17 shear test configuration.

To calculate the shear strength of samples, the load required to shear the specimen was divided by the area of the sheared edge (Equation 12). The product of the thickness of the specimen and the circumference of the punch (C_P) produced the area of the sheared edge (Equation 11). The thickness of specimen was calculated as an average ($\bar{T}$) due to irregularities present on the sample. Thicknesses were measured at five different points following the circular shape of the sample (Figure 15).

Equation 11: $Shear\ Edge = \bar{T} * C_P = SE$

Equation 12: $Shear\ Strength = \frac{F}{SE} = \tau$

2.6.6. Shear Testing Sample Preparation

Samples for shear testing were prepared utilizing a polycarbonate sheet that was laser cut to match sample dimensions described by ASTM D732 [30] and PTFE sheets to ensure easy release from the mold. Then, utilizing a vulcanizer, a mass of sample beads was added and heated slowly in the mold until the sample started to overflow onto the PTFE release film. This ensured samples were as flat as possible and met compression standards for polymeric agglomeration an example of the shear test samples in shown in Figure 15.

Figure 15: PCL Shear test sample prior to testing.

The uniformity allowed for more accurate testing and failure as they were exposed to shear. Prior to testing, a center hole was drilled via drill press to allow for the pin in the shear mechanism to smoothly pass through the specimen. During testing, the weight of the pin was negligible to the overall shear stress experienced by the samples. Samples were clamped tightly between the two steel plates and the sample was secured in the center of the testing apparatus due to the center hole alignment of the specimen and the pin (Figure 14)

2.6.7. Split-Hopkinson Pressure Bar Testing

SHPB testing was performed on the complete range of PCL samples with an aluminum bar to observe dynamic loading through dynamic flow stress, and strain rates change within samples. Samples were tested at three strain rates to observe variance in dynamic flow stress to adequately describe PCL and through softening of solvent and reinforcement from ANF under a dynamic load. An example of the split-Hopkinson pressure bar system used in shown in Figure 16

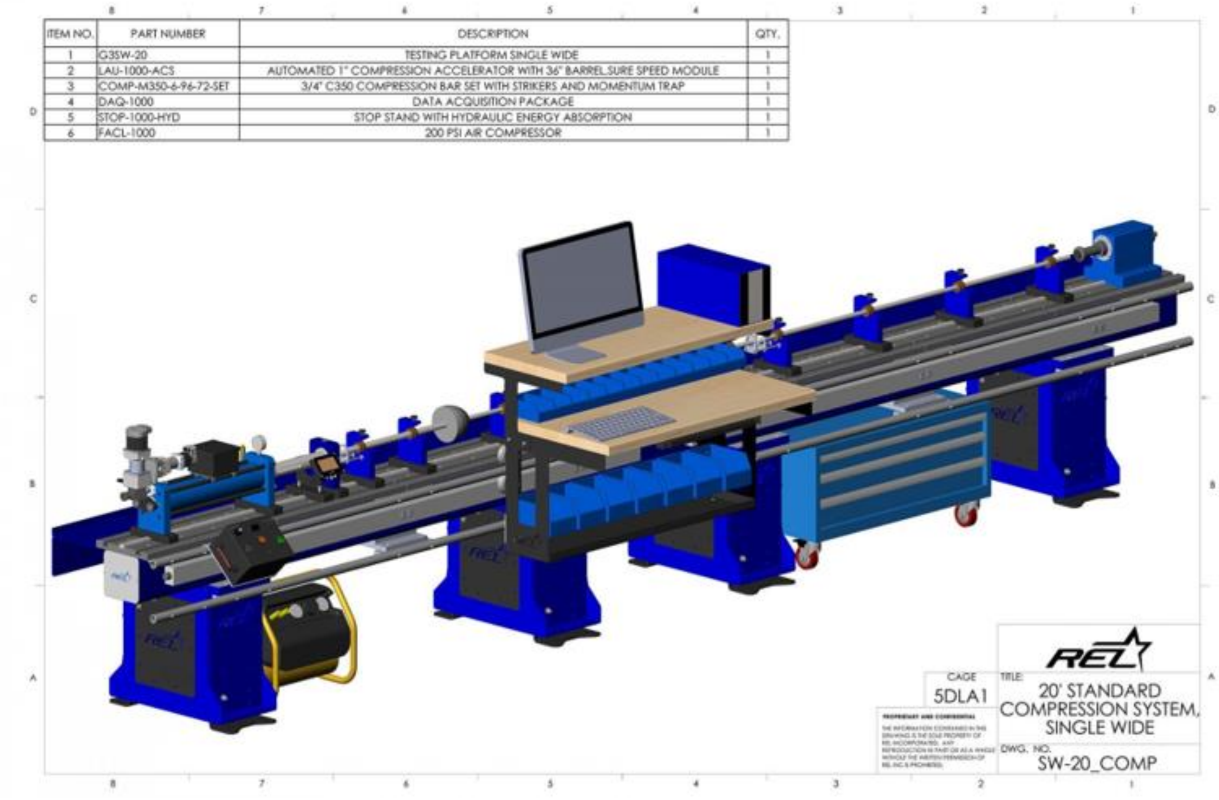

ITEM NO.	PART NUMBER	DESCRIPTION	QTY.
1	G3SW-20	TESTING PLATFORM SINGLE WIDE	1
2	LAU-1000-ACS	AUTOMATED 1" COMPRESSION ACCELERATOR WITH 36" BARREL,SURE SPEED MODULE	1
3	COMP-M350-6-96-72-SET	3/4" C350 COMPRESSION BAR SET WITH STRIKERS AND MOMENTUM TRAP	1
4	DAQ-1000	DATA ACQUISITION PACKAGE	1
5	STOP-1000-HYD	STOP STAND WITH HYDRAULIC ENERGY ABSORPTION	1
6	FACL-1000	200 PSI AIR COMPRESSOR	1

Figure 16: SHPB system used for polymer composite testing manufactured by REL.

Prior to testing the PCL and PCL/ANF samples, trial runs were conducted to ensure that data obtained from the samples could be accurately calculated and in turn observed through several calculations. The end goal of the testing was to obtain dynamic flow stress vs strain rate in the samples and in turn, how this data changed with increasing ANF weight percentages. Dynamic flow stress is the instantaneous stress required for continual plastic deformation of material. By comparing dynamic flow stress, and strain rates of the specimen, the deformation patterns and failure mechanisms can be observed between sample types. Calculating the dynamic flow stress and strain rates required analysis of voltage data acquired from strain gages placed on the incident and transmission bars Figure 17 [31].

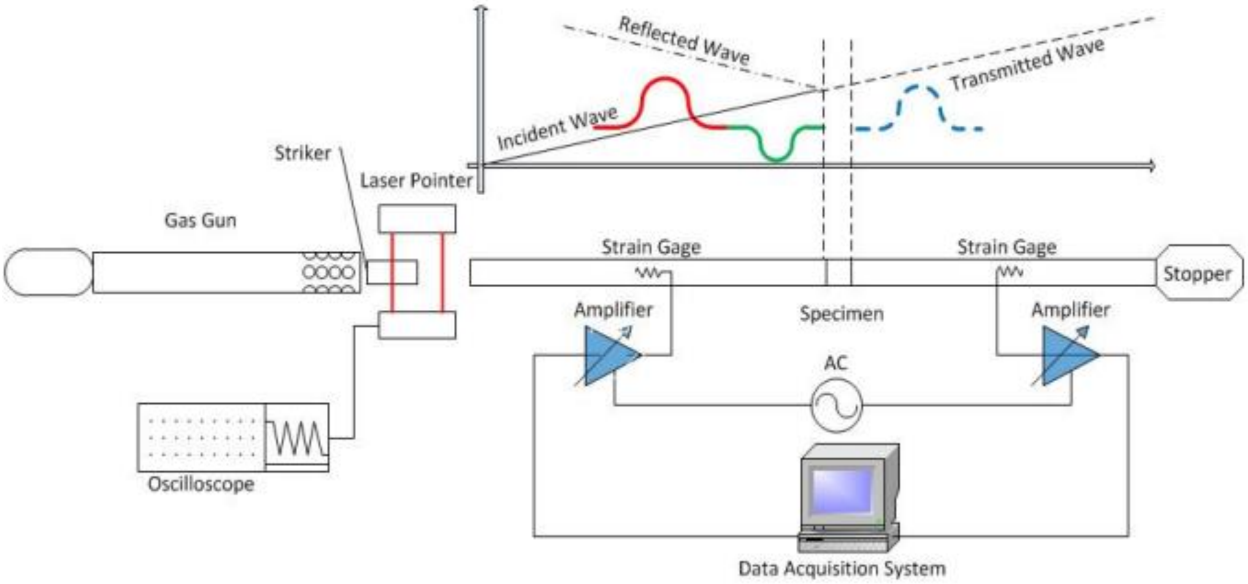

Figure 17: SHPB diagram depicting strain gage location and pulse traveling concept.

After the striker bar is fired from the gas gun and impacts the incident bar, the incident wave travels through the bar and passes into the specimen. After passing into the specimen, a transmitted wave and a reflected wave propagate into the transmitted bar and incident bar respectively. These pulses are measured by strain gages located in the middle of both the incident and transmission bars. The pulses that are recorded are measured in voltages and are converted through Equation 13 to obtain incident, reflected and transmitted strains.

$$\text{Equation 13: } Inc, Ref, Trans\ Strain = \left({-\left(\frac{v_{strikerbar}/2}{\mathrm{E}_{bar}}\right)} \Big/ {\overline{\delta}} \right) * V_{Inc,\ Ref,\ Trans} = \varepsilon(t)_{Inc,\ Ref,\ Trans}$$

$\overline{\delta}$ represents the average of the incident pulse once it has reached first cycle equilibrium. After calculating the strain for incident, reflected and transmitted pulses, strain rate, strain, stress, true strain rate, true strain, and true stress can be calculated following Equation 14 through Equation 19.

$$\text{Equation 14: } Strain\ Rate = \left(\frac{2*E_{bar}}{l_{sample}}\right) * \varepsilon_{Ref} = \dot{\varepsilon}(t)$$

$$\text{Equation 15: } Strain = \varepsilon(t_0) + (t - t_0) * \dot{\varepsilon}(t) = \varepsilon(t)$$

$$\text{Equation 16: } Stress = \left(\frac{-1000*E_{bar}*\frac{\pi}{4}*(D_{bar})^2}{\frac{\pi}{4}*(D_{sample})^2}\right) * \varepsilon(t)_{Trans} = \sigma(t)$$

$$\text{Equation 17: } True\ Strain\ Rate = {\dot{\varepsilon}(t)} \Big/ {(1 - \varepsilon(t)} = \dot{\varepsilon}(t)_{true}$$

$$\text{Equation 18: } True\ Strain = -\ln\big(1 - \varepsilon(t)\big) = \varepsilon(t)_{true}$$

$$\text{Equation 19: } True\ Stress = \sigma(t) * (1 - \varepsilon(t) = \sigma(t)_{true}$$

An aluminum bar was also chosen for testing PCL and PCL/ANF composites due to similar young’s modulus but having a higher mechanical impedance than the samples. High-speed camera (HSC) recordings aided in characterizing the impact deformation, impact duration and the unique non-uniform deformation mechanism of the samples. HSC also aided in PCL characterization deformation due to face force imbalances caused by modulus difference between the bar and sample. Face forces describe the balancing of forces on the two faces of the sample during wave propagation. Ideally, the incident face force (Equation 20) should equal the transmitted face force (Equation 21) to show the sample was fully loaded and experienced the maximum amount of stress and strain possible. To aid in prolonged loading and stress distribution in the sample, a copper pulse shaper with a thickness of 0.5 mm and diameter of 7 mm was utilized.

Equation 20: $$Inc\ Face\ Force = \left(-1000 * E_{bar} * \frac{\pi}{4} * (D_{bar})^2\right) + (\varepsilon(t)_{Inc} + \varepsilon(t)_{Ref})$$

Equation 21: $$Trans\ Face\ Force = \left(-1000 * E_{bar} * \frac{\pi}{4} * (D_{bar})^2\right) + \varepsilon(t)_{Trans}$$

2.6.8. Split-Hopkinson Pressure Bar Sample Preparation

SHPB testing samples were prepared by copper tubing that molded samples with the dimensions to best observe the materials reaction under rapid loading. Samples molded for SHPB testing were approximately 8.00 mm in diameter and 6.00 mm in thickness. Samples were heated to approximately 90 ˚C and placed on PTFE films to allow for easy release. PCL and PCL/ANF beads were added in small layers to allow for proper heating of the sample after which the layers of PCL or PCL/ANF were compacted to remove potential voids within the sample before further beads were added. After the full volume of sample mold was used for the required specimen dimensions, the sample was inserted into a vulcanizer to ensure two parallel flat surfaces and to increase sample uniformity (Figure 18).

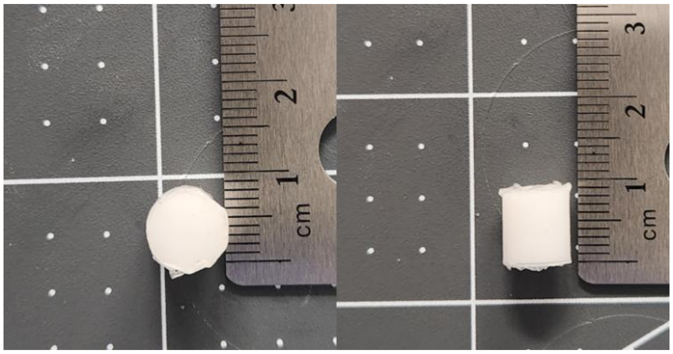

Figure 18: SHPB samples.

Sample uniformity and sample face parallelism was an important factor for SHPB sample synthesis. These factors affect the stress pulse propagation from the aluminum testing bars into the softer PCL samples. PCL also exhibited a unique loading property through plastic deformation that pre-loaded samples and further ensured that the two faces of SHPB samples were parallel during testing.

3. Discussion of Results

3.1. Tensile Testing

To more accurately assess the effectiveness of doping PCL with the varying weight percent of ANF as well as the effect of the solvent on the polymer matrix, two strain rates were utilized for tensile testing. Primarily, a strain rate of 4 mm/min was used for classical quasi-static analysis. This testing allowed for the observation of a phenomenon unique to polymers notated as Hermans' orientation function [32] and the changes among the sample sets. Secondarily, a strain rate of 240 mm/min was used to observe performance of samples at a higher loading rate. The main goal of this testing was to observe the tensile properties of polymer while observing the effect of Hermans' orientation and cross-linking of polymer chains. By inducing a higher strain rate, the samples experience failure much quicker. This further allows for comparison within the sample subsets to analyze how the samples changed in failure when experiencing larger strain rates. Figure 19 represents the results of testing native PCL, solvent dissolved PCL and PCL at one and two-weight percent ANF for the associated Young's modulus at two strain-rates.

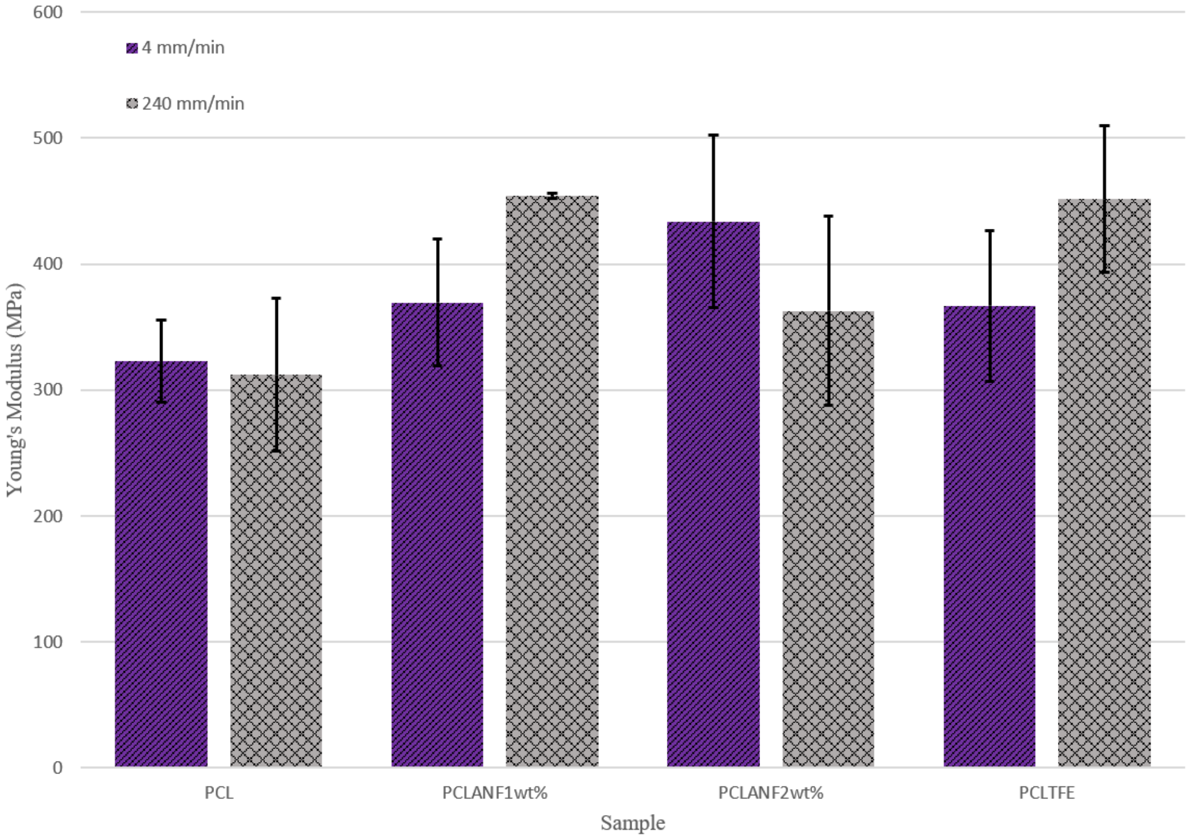

Figure 19: Young's modulus averages for the complete range of PCL samples tested at 4 mm/min and 240 mm/min.

Figure 19 shows that at a crosshead velocity of 4 mm/min, the reinforcement of ANFs within PCL provides a substantial increase in stiffness to the material of approximately 34 % for two-weight percent ANF. However, at a crosshead velocity of 240 mm/min, the one-weight percent ANF sample performed the best in relative stiffness by increasing approximately 45 % relative to native PCL. Similarly, PCLTFE samples behaved similarly to one-weight percent ANF samples. This suggests that at one-weight percent ANF, little alteration is occurring to create reinforcement to the PCL matrix to tensile forces. To calculate the young's modulus of samples, the raw data was imported and converted to true stress and true strain values (Figure

20A). Following this conversion, the linear portion (circled in red) was fitted with a linear trendline with a minimum R^2 of 0.98 as shown in Figure 20B.

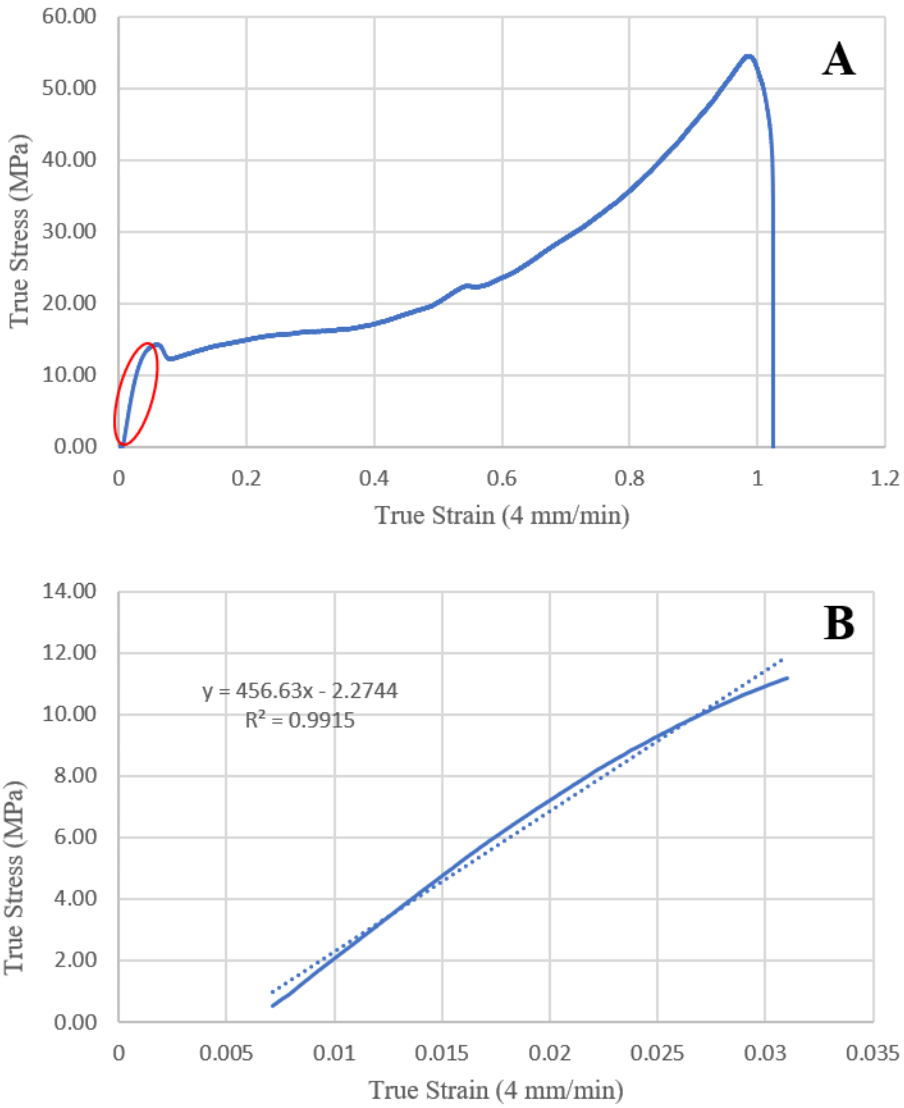

Figure 20: (A) True stress and true strain for 4 mm/min tension test. (B) Linear trend fitting in Excel for young's modulus calculation.

Figure 20A shows the unique stress strain interaction that occurs for polymer tensile loading. Comparing Figure 20A to Figure 21 shows common stress strain graphs for polymers versus metals. Key distinctions that occur are most noted in how the samples experience yielding failure. Polymers have a distinct trend that sustains stress as strain increases. This trend highlights the elongation and ductility of the materials. Similarly, ultimate stress of a polymer is where the sample experience failure. Metals however, trend upwards in yield, showing an increased load supported because the material is not elongating to compensate for the increase load. Furthermore, ultimate stress does not indicate that the sample has fractured, failing sometime after achieving ultimate stress.

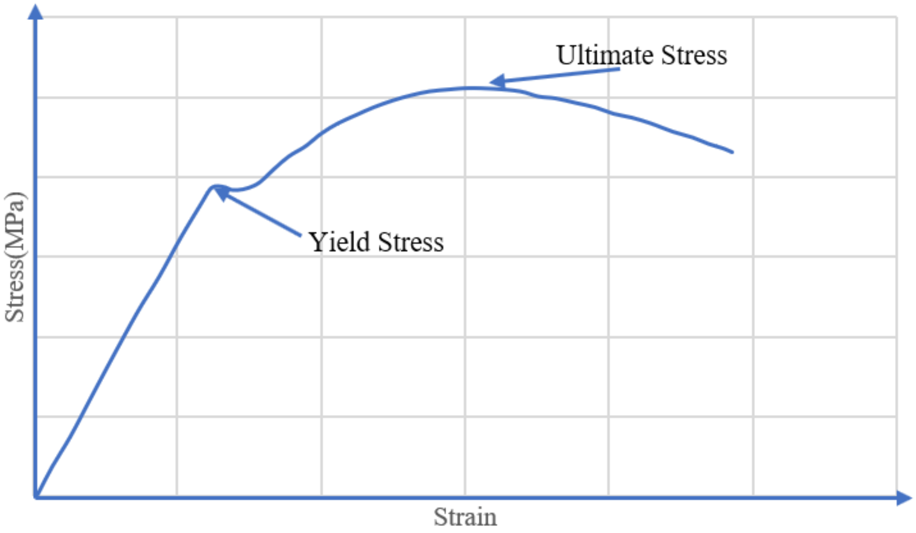

Figure 21: Typical stress strain behavior for metal in tensile loading.

Comparing Figure 20A to Figure 21 further accentuates the need for utilizing true stress and true strain equations for calculating the load sustained by PCL and the sample constituents. Due to the very large elongation factor of PCL, the load sustained greatly increases for ultimate stress, where the sample has increased greatly in length and decreased in cross-sectional area.

Figure 22 further describes the reinforcement of ANFs in the PCL matrix through ultimate and yield stress.

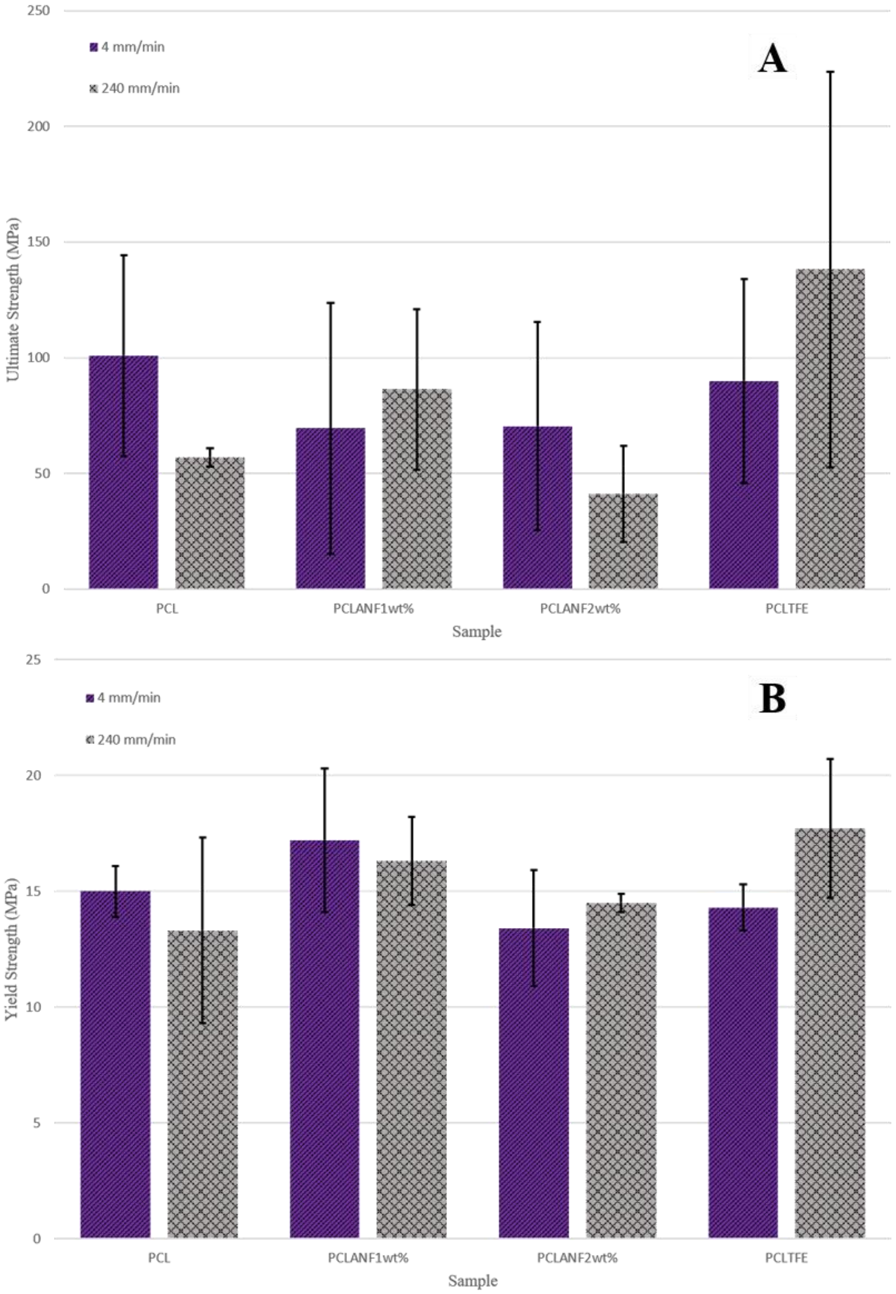

Figure 22: Young’s modulus averages for the complete range of PCL samples tested at 4 mm/min and 240 mm/min.

Figure 22 shows across all sample that ultimate strength decreased when compared to native PCL at the crosshead velocity of 4 mm/min. However, at a crosshead velocity of 240 mm/min, PCLTFE performed the best yet with substantial outliers to its performance. The next best performing sample was one-weight percent ANF showing an increase in ultimate failure by approximately 51 %. Where two-weight percent marginally decreased between both testing methods by 10.8 % and 27.8 %. This ultimate failure decrease likely occurs to micro and nano-fragmentation/voids and poor fiber to matrix adhesion that becomes more relevant as samples elongate to extreme ranges and the necking cross-sectional area decreases significantly. The voids in turn cause early failure in the samples while their stiffness shows an increase from Figure 22. Extreme necking frequently occurred for the PCLTFE samples, likely due to a ductility increase allowing for superior elongation in the dog bone samples. However, in some instances, early failure was observed due to air gaps from sample preparation. This in turn lead to early failure for some samples causing an extreme standard deviation with incredibly high and low peak elongation. An example of this of the tensile samples is shown in Figure 23 as well as the extreme necking region and air gap failure.

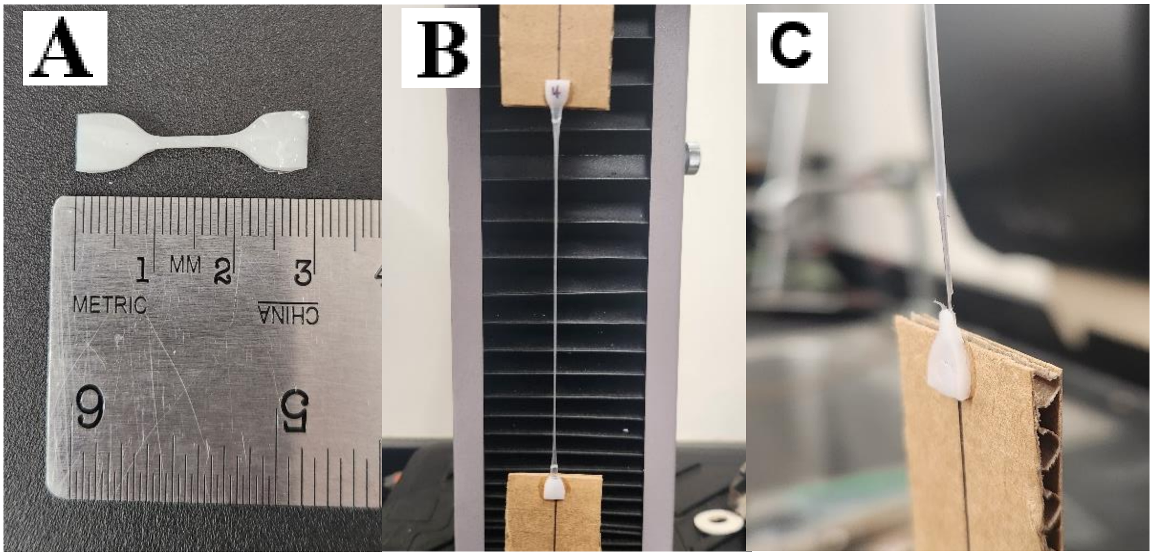

Figure 23: (A) PCL dog bone sample for prior to tensile testing. (B) Extreme elongation of PCLTFE tested at 240 mm/min. (C) Air bubble necking fragmentation.

For elongation standards during tensile testing, a maximum increase in elongation compared to PCL was found to be 45 % for PCLTFE samples when tested at 240 mm/min. This in turn aids in the conclusion that upon being dissolved by TFE; PCL softens, allowing it to have greater elongation capability and corresponding increase in true yield stress and true ultimate strength. Upon the addition of aramid nanofibers, sample stiffness did increase when tested at the slower 4 mm/min but decreased when tested at the quicker 240 mm/min at two-weight percent ANF. This is again, likely due to fragmentation on matrix to fiber adhesion difficulties that propagated early failure for the sample. In turn, the two-weight percent samples seem to perform on level with PCL or worse due to fragmentation of voids created from the ANF, especially due to PCL's elongation properties. Further studies should be performed to aid in categorizing ANF adhesion to polymer matrices to aid in the fabrication of nanofiber composite materials.

3.2. Compression Testing

Compression testing provides insight into a material's performance in terms of compressive modulus and compressive yield strength. Compressive properties are essential to understanding SHPB testing and wave propagation. The compressive modulus of the material directly affects the dynamic flow stress and strain rate of the samples. Similarly, understanding the quasi-static behavior of the samples aids in understanding the wave propagation properties of the sample. Figure 24 provides insight to the compressive yield strength and compressive modulus for the complete range of PCL samples.

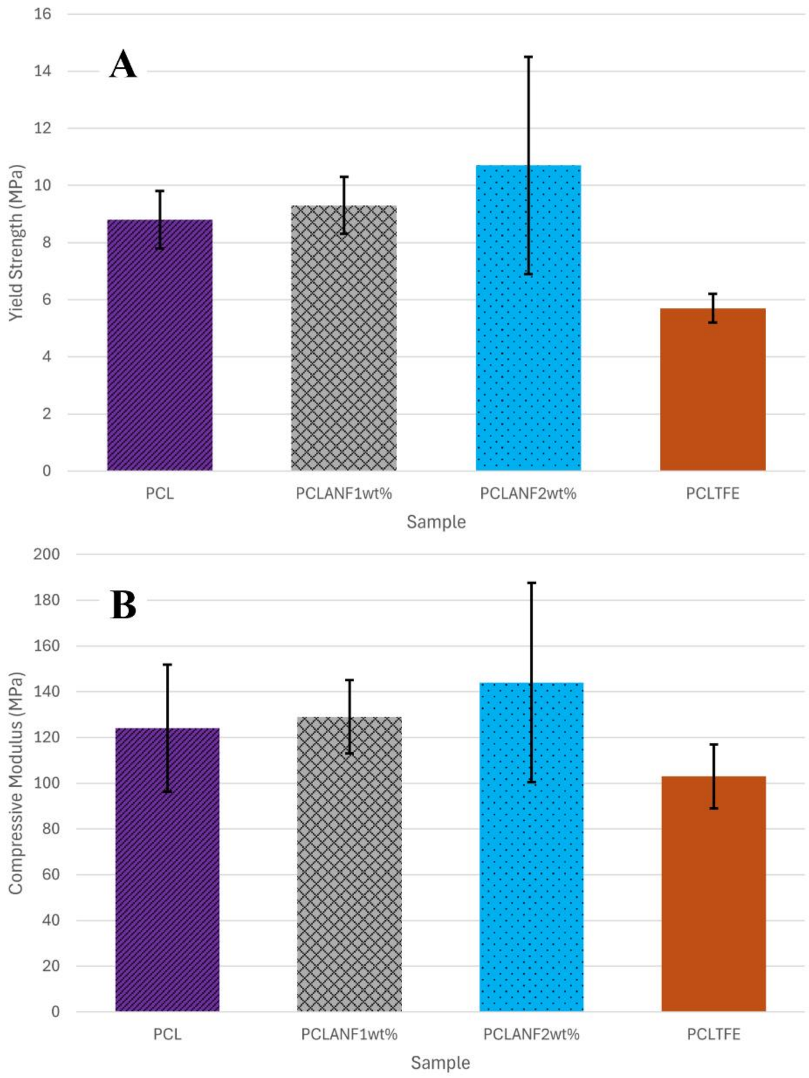

Figure 24: (A) Compressive Modulus for the complete range of PCL samples. (B) Compressive yield strength for the complete range of PCL samples.

Compressive testing showed a modest increase in Modulus and Yield as ANF weight percent is increased in the samples’ composition. This provides information that upon increasing ANF, the stiffness of PCL samples increases in compression despite TFE softening. While the increase in stiffness compared to PCL appears somewhat minimal, the increase from PCLTFE samples is much more significant. The compressive modulus of one and two-weight percent

ANF compared to native PCL increased by 4 % and 16 % respectively, and yield increased similarly at 6 % and 22 % respectively. When comparing the reinforced samples to PCLTFE the modulus increased by 25 % and 40 % respectively and yield increased by 63 % and 87 % respectively. This data in turn shows that upon the addition of ANF to a PCL matrix, despite TFE solvent softening, a compressive reinforcement is shown and is significant. This is indicated by the stated substantial increase in compressive modulus. This is likely supported through random distribution of ANF in the matrix, allowing for an increased load as the ANFs provide load distribution and support to the composite [24]. Furthermore, ANF adhesion to the matrix is much less critical in compressive testing for PCL where elongation of samples is not an impacting factor to the performance of the samples. Due to the impressive elongation properties of the samples, it is likely that the ANF reinforcement simple could not aid at the large strains that were observed. Whereas the minimal crosshead differences in compressive testing allowed for better fiber to matrix support under loading.

3.3. Shear Testing

To mechanically characterize the complete range of PCL samples, shear testing was also performed. Some difficulties were observed during this testing due to the inherent nature of polymers. The main factor that contributed to issues in data collection was the inherent elongation properties of PCL, causing portions of the specimen to remain incredibly thin and intact after the peak load of shear developed. This in turn caused a sustained load to be present even after the maximum load rapidly dropped off. This condition is addressed by the ASTM standard and calls for the removal of the specimen after peak load development and the rapid load decrease. The maximum shear strength for the samples is reported in Figure 25.

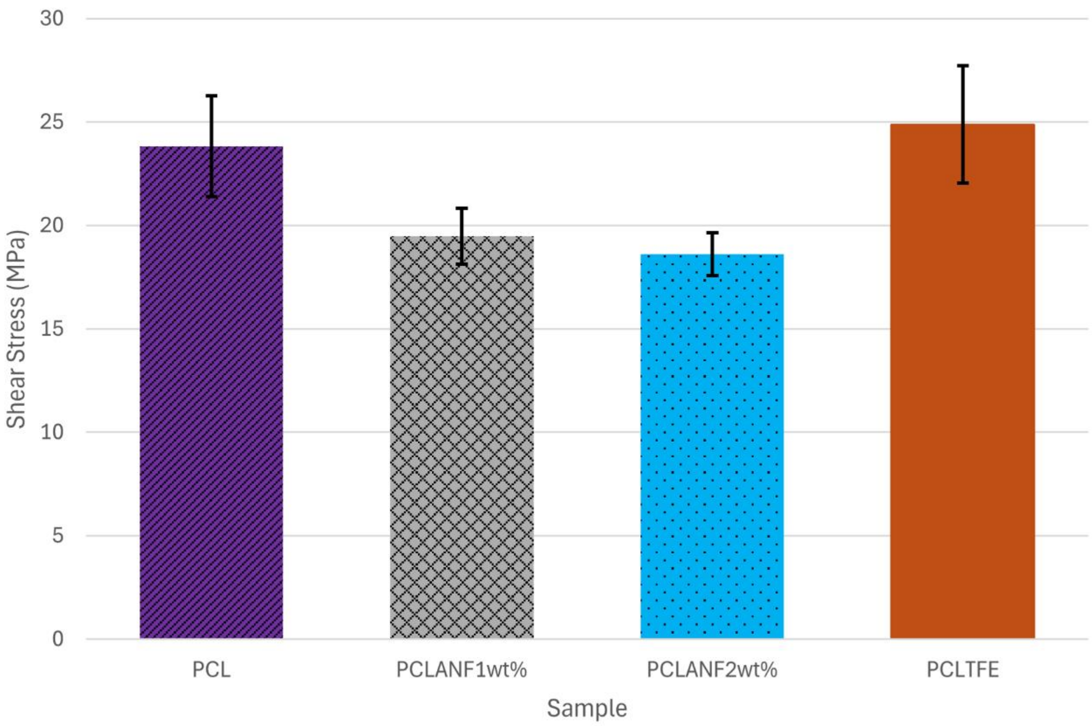

Figure 25: Maximum shear strength for the complete range of PCL samples.

Testing in shear strength for PCL samples yielded similar results to tensile testing. PCLTFE showed similar performance to PCL, increasing in True Shear Strength by only 4 %. However, both one and two-weight percent ANF composite samples decreased in their maximum shear strength by 18 % and 22 %. The reinforced sample poor performance likely arises from the elongation properties of PCL and the matrix to fiber adhesion issue that occur from elongation of a polymer matrix. As the polymer attempts to lengthen through Herman's orientation, ANF present in the material act and create breaks in the anisotropic properties and interfere with any tensor properties that strengthen both PCL and PCLTFE in this testing methodology.

3.4. Split Hopkinson Pressure Bar Testing

Based on the compression testing, SHPB was performed to dynamically test the range of PCL samples for wave propagation, axial compression, and dynamic flow stress at varying strain rates. Based on the increasing trend in compressive modulus, it was expected that an increase in dynamic flow stress would be seen in the reinforced samples. To aid with this testing, HSC was also utilized to capture the loading of samples, first cycle compression and first cycle impact duration. The main concern and reasoning for HSC was differences between the modulus of the PCL samples and the available bars for SHPB testing. With the differences in modulus, face forces during the loading of the sample were calculated and noted to be consistently inequal. In turn, HSC provides imaging to this error, and allows for further and detailed explanation of this unique dynamic loading. The dynamic loading of polymer samples becomes difficult due to the plastic deformation that occurs prior to full loading and permanent deformation of the samples. While this caused further difficulties with face force equilibrium, it did aid in reducing potential errors that could have occurred if the two faces of the sample were not perfectly parallel. This allowed for excellent wave propagation into the samples due to their inherent alignment during testing.

To categorize the testing parameters for SHPB testing, a range of striker bar velocities was chosen based on pressure in the attempt to provide the widest range possible for high strain rate outputs. The four categories for pressure were 15 psi, 20 psi, 30 psi, and 40 psi which yielded striker bar velocities of approximately 10 m/s, 15 m/s, 20 m/s, and 25 m/s respectively. With these four categories of striker bar velocities, three main categories of strain rates were obtained that successfully classified the complete range of PCL sample at high strain rate. The strain rate ranges for this testing were categorized as 1500 s^{-1} ~ 2500 s^{-1}, 2500 s^{-1} ~ 3500 s^{-1}, and 3500 s^{-1} ~ 4500 s^{-1}. The true flow stress data for these strain rates is shown in Figure 26 and true stress true strain graphs for strain rate groups for sample groups can be found in Appendix A.

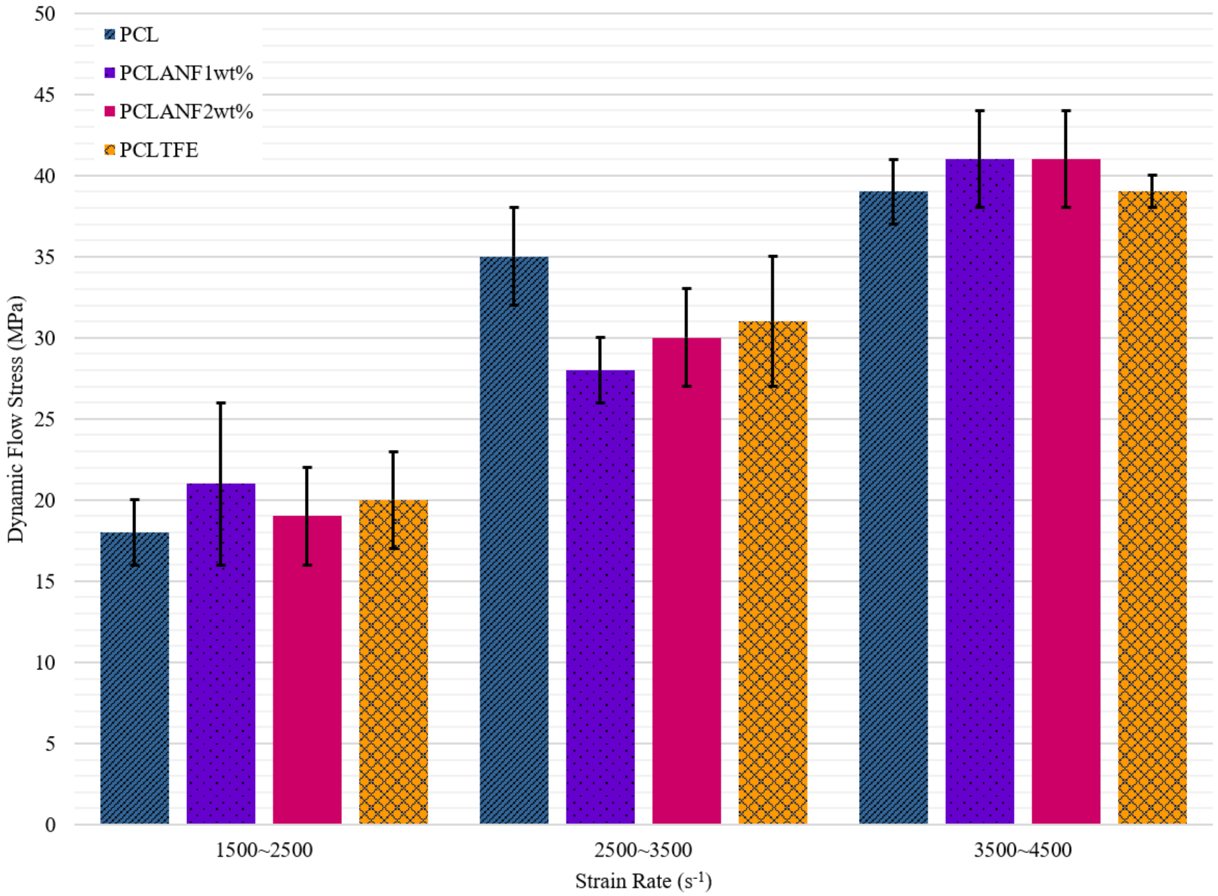

Figure 26: Dynamic flow stress average based on sample and strain rate for the full range of PCL samples.

Figure 26 shows that as the strain rate increased, the true flow stress also increased incrementally. Most notably, there is a significant decrease in true flow stress achieved at 2500 s $^{-1}$ ~ 3500 s $^{-1}$ for all samples when compared to PCL. While it is expected that PCLTFE would sustain less flow stress compared to PCL, it is unexpected that the ANF reinforced samples would show a marginal drop in flow stress. This expectation arises from the modulus changes that were seen in compressive testing. In turn, PCL samples demonstrated the co-occurrence of strain rate strengthening and adiabatic thermal softening at high strain rates [33]. Furthermore, the effects of thermal softening were the most impactful at 2500 s $^{-1}$ ~ 3500 s $^{-1}$. Due to this significance at the strain rate of 2500 s $^{-1}$ ~ 3500 s $^{-1}$, axial compression and impact duration also saw the most fluctuation when compared to PCL. Axial compression decreased by approximately 37 % and 16 % for one and two-weight percent ANF respectively. Meanwhile, only the two-weight percent sample tested at 2500 s $^{-1}$ ~ 3500 s $^{-1}$ saw any significant changes in impact duration, increasing in time by approximately 16 %. This data was calculated utilizing ImageJ and HSC to capture the first cycle loading of the samples at varying strain rates. An example of the first cycle compaction is shown in Figure 27.

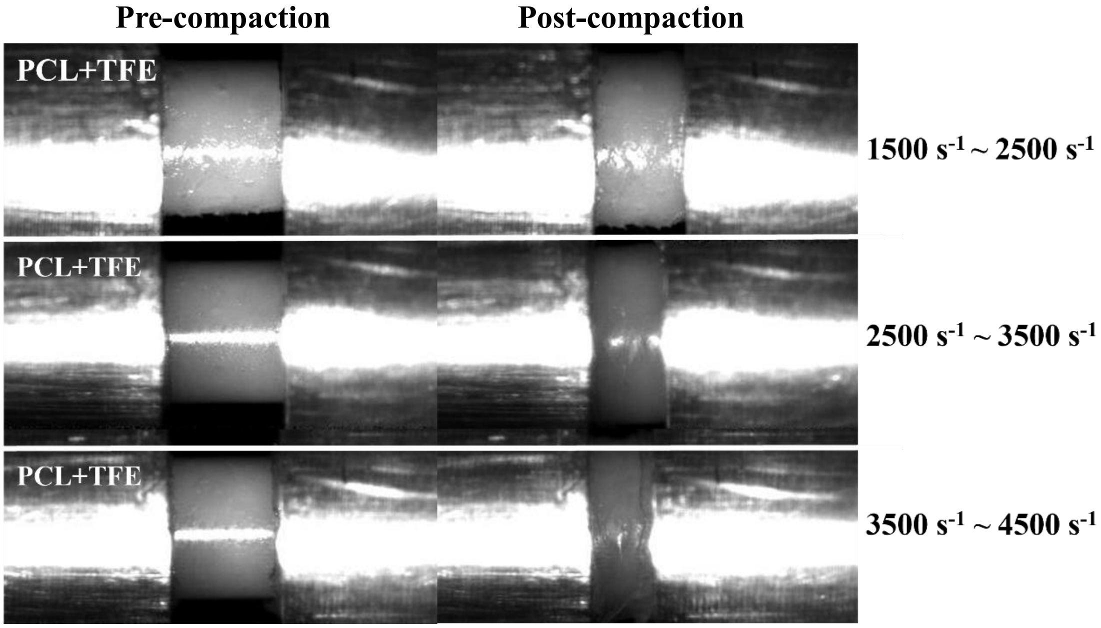

Figure 27: PCL +TFE first cycle compaction for the full range of strain rates tested.

To characterize the first cycle compaction of the samples, HSC was used and captured at a frame rate of 210 kfps. Through ImageJ, first cycle compaction could be measured through known specimen dimensions for the pre-compacted state for the post-compacted state to be quantified. Similarly, the frames captured by the HSC allowed for impact durations to be calculated to observe changes in loading time and strain rate in the samples. The compaction percentages for each sample tested in strain rate grouping is shown in Figure 28.

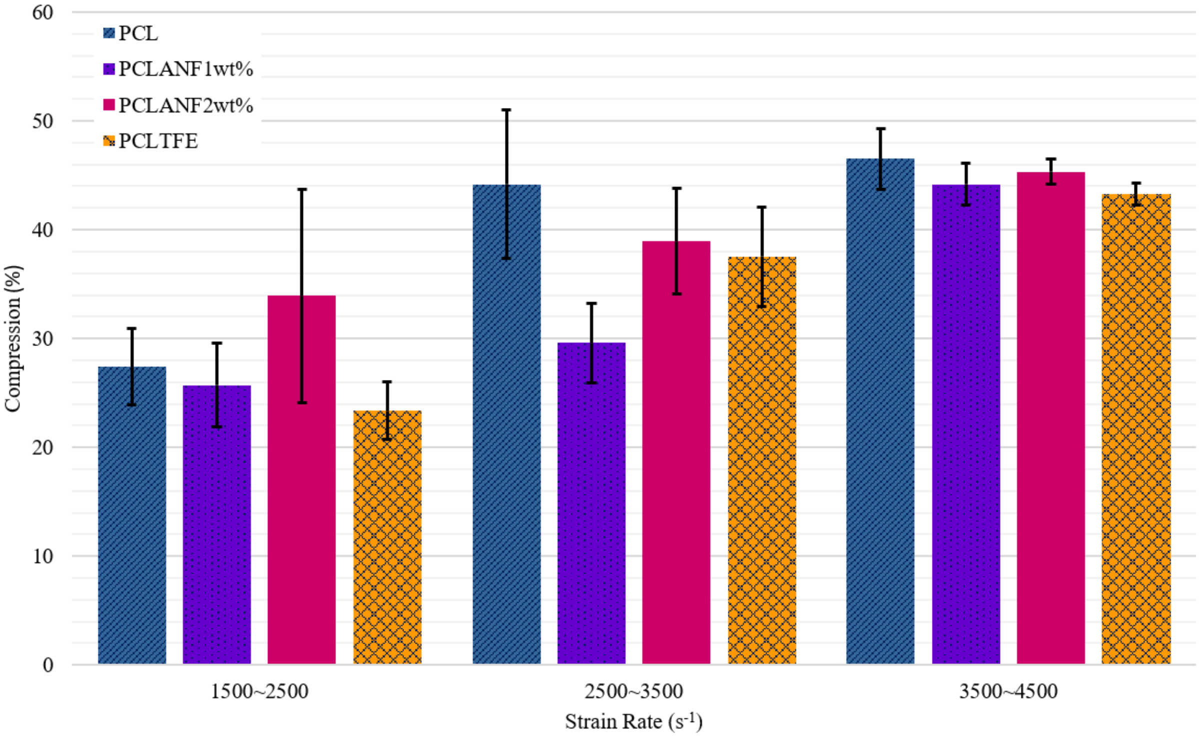

Figure 28: Compression percent for the complete range of PCL samples grouped by strain rate.

In turn, at low strain rates, PCL saw minor changes in its capability to sustain dynamic load due to the ANF doping. However, at high strain rates, where thermal softening heavily occurs due to the large energy input into the sample, no distinct variation in flow stress occurs. This is due to the sample achieving a minor fluidic state due to the low glass transition temperature and melting point of PCL where the fibers cannot support a fluidic matrix.

4. Conclusion

Through this mechanical characterization study, PCL mechanical properties were observed and measured through four mechanical tests. The first test performed was tensile testing. This testing concluded that ANF was able to increase the stiffness of PCL by approximately 34 % when conducted at a slow strain rate of 4 mm/min. At faster strain, PCL did not see the same stiffness reinforcement, which may be attributable to the ANFs creating voids in the material. Testing also showed that upon being dissolved in TFE, PCL softened and had greater elongation properties. It can be concluded that the elongation properties of PCL perform well with fiber reinforcement based on the observed increase in tensile strength. The significant elongation property likely causes matrix to fiber interaction to propagate early failure through voids as the matrix elongates and separates from the suspended fibers. This conclusion is aided by the decreased ultimate and yield stress supported by reinforced PCL samples by the early failure.

The second test performed was compressive testing. This testing provided compressive modulus of the four samples. This testing did provide an increase in compression modulus by approximately 16 % for 2 weight percent samples. This reinforcement likely occurs due to the minimal crosshead deflection that occurred during compressive testing compared to the tensile testing elongation. The minimal deflection allowed for the PCL matrix to be supported by the fibers.

The third test conducted was shear testing. Like the tensile testing, large cross head deflections were observed. In this testing, a decrease in shear load was found for reinforced samples by approximately 18 % and 22 % for one weight and two weight percent ANF respectively. Having similar decreases in sample performance between tensile and shear testing, aids in the conclusion that the PCL matrix performs poorly with nanofiber reinforcement due to its elongation properties.

The fourth and final test was SHPB testing. This testing was the most comprehensive test of the four that were used to characterize the performance of ANF reinforcement. At low strain rates, PCL reinforced with two weight percent ANF was observed to support a high true flow stress compared to PCL. Furthermore, the reinforced samples at low strain rates showed decreased axial deformation by approximately 37 % and 16 % for one and two weight percent ANF respectively due to the stiffness increases shown from the compressive test. However, at higher strain rates, the reinforced sample either performed worse or the same as PCL. This occurs from thermal softening of PCL due to its low glass transition temperature and melting point creating a fluidic sample that cannot be reinforced or stabilized by nanofibers.

The synthesis of the self-healing polymer yielded inconclusive results from fabrication failures. This likely arises from multiple issues. One of the most prevalent issues is the lab grade purity that can be achieved by professional laboratories compared to campus equipment. While the monomer synthesis was generally successful, it is likely that the small impurities in the synthesized monomer inhibited the self-healing polymer quenching process. The mechanical characterization of PCL ANF composite still provides a strong foundation to continue preliminary testing to apply towards future polymer composites.

5. Future work

Future studies will be performed at higher weight percent ANF to observe peak performance of composites. It is likely that increasing the concentration of ANF in PCL will increase the compressive modulus of PCL and also provide benefits in dynamic loading. Future investigations aim to study ANF polymer composites in body armor and protections applications. Future work also includes ANF interactions with other classifications of polymers. Investigating ANF reinforcement in different polymer classifications would classify the best matrix and fiber interaction. Similarly, to increase matrix to fiber interaction, surface area modification of ANF will be investigated.

It is likely that rigid plastic polymers would obtain strong benefits for ANF reinforcement. Polymer composites reinforced with ANF have shown to have increased toughness and resilience but suffered in tension and shear testing. In applications where elongation of the matrix was studied, voids seemed to propagate from ANF doping, creating early failure. Rigid plastic polymers would provide a stiffer matrix for ANF reinforcement because of minimal elongation properties. Studying a polymer with higher melting and glass transition temperatures would benefit high energy dynamic testing. By incorporating a thermally resistive polymer, higher strain rates could be tested to show ANF reinforcement under greater dynamic load.

Continuing these studies could prove useful in the development of reinforced textile materials. The benefit of creating reinforced polymer textiles is the ability to craft unique structures and patterns through electrospinning applications. ANF reinforcement could further benefit end properties of electro spun materials while benefitting from ANF biocompatibility. Overall, ANF provide a strong candidate for nanocomposite materials.

6. Experimental Methods

6.1. Aramid Nanofiber Fabrication

PPTA fibers (*0.6 g)* and KOH *(0.9 g)* were added to *300* mL of DMSO. DI water was then added in a specific volume ratio to DMSO of 1:25 respectively. This solution was magnetically stirred for a minimum of 4 hours to for ANF/DMSO solution. As the solution was allowed to stir, the color of the solution transitioned from clear, to slight yellow tint, to a dark red; indicating that the deprotonation of the aramid fiber was completed. The structural restoration of ANFs was then accomplished by utilizing DI water as a proton donor for the system. To complete the structural reconstruction of ANFs a specific volume ratio of DI water to ANF/DMSO solution of 2:1 was utilized. This yielded a uniform ANF/DMSO/H_2O solution after being stirred with a magnetic stir bar for a minimum of 1 hour. Further color transitions occurred that signified the completion of the structural restoration of the aramid fibers as the solutions changed from a dark red, back to a slight yellow tint [14].

Filtration of the fibers was performed utilizing 0.2 µm pore rapid flow Nalgene filter systems to remove excess large fiber distributions. After removing the unwanted large fibers, the filtered material was washed using excess DI water and methanol leaving a solution of ANF/DMSO/H_2O/CH_3OH. To collect the suspended fibers, solvents were removed using a vacuum oven in a two-step process. Initial solvent removal occurred by placing the solution under vacuum at 510 mmHg and heated to 85 °C to remove H_2O and CH_3OH, leaving a solution of ANF/DMSO. This solution was then transferred to scintillation vials where the oven could be heated to a higher temperature of 150 °C and a vacuum of 510 mmHg until the scintillation vials were left as dried ANF.

6.2. PCL/ANF Composite Fabrication

TFE (20 mL) was introduced into dried ANF scintillation vials and left to sonicate for a minimum of 2 hours. After sonication, 50 µL was placed onto an SEM stub and left in a fume hood to completely dry. After the stub dried, the sample was gold coated for SEM analysis where a minimum of five micrographs would be taken at relatively large-scale imaging for better approximation of fiber area fractions. These micrographs were then used to convert an average area fraction into a volume fraction to estimate the concentration of ANF dispersed in solution. Based on the concentration of TFE/ANF solution, a double weight percent calculation was performed to produce dispersible and formable beads of PCL onto wax paper.

The first weight percent calculation performed was weight percent of PCL in TFE in solution. This weight percent was important as the weight percent of PCL would dictate the viscosity of the beads and in turn how easily manipulated the beads were. Lower weight percent yielded solution that was runny and yield beads that were difficult to manipulate into sample molds. Higher weight percent yielded solution that was difficult to remove from beakers via syringes. In turn, the general weight percent chosen for PCL in TFE was 10 weight percent.

The second weight percent calculation performed was ANF in PCL. This weight percent would dictate the performance of the samples for all mechanical testing and was performed through the concentration of the TFE/ANF solution to the amount of PCL required for the desired viscosity of the beads. The sample would then be heated to approximately 60 °C in a water bath and sonicated to promote random and even distribution of fibers within PCL. Sample solutions were exposed to heat and sonication for a minimum of 30 minutes.

6.3. Monomer synthesis

In argon atmosphere, magnesium turnings (*3.3* g, *0.14* mol), anhydrous lithium chloride (*5.3* g, *0.12* mol), a catalytic amount of iodine (*0.05* g, *0.2* mmol) and *300* mL anhydrous tetrahydrofuran were added to a 500 mL three-neck flask. The reaction mixture was heated to reflux and 2-bromo-4-methylanisole (*25.0* g, *0.12* mol) was added dropwise. After stirring for another 1 hour at room temperature, allyl bromide (*22.6* g, *0.19* mol) was added slowly. The reaction mixture was then stirred overnight and quenched with saturated ammonium chloride aqueous solution. The crude product was purified through silica gel column chromatography (n-hexane) to give colorless liquid (*17.0 g, 84* %) [1].

6.4. Polymer synthesis

In a THF-free glovebox, a toluene solution (*150* mL) of AP (*740* mg, *5* mmol) was charged into a three-necked flask with a magnetic stir bar. The flask was set in a water bath (*20* °C) and connected to a well-purged Schlenk ethylene line. Ethylene (*1* atm) was introduced into the system and was saturated in the solution by stirring for 2 min. A toluene solution (*2* mL) of $(C_5Me_4SiMe_3)Sc(CH_2C_6H_4NMe_2\text{-}o)_2$ (*5.1* mg, *0.01* mmol) and $[Ph_3C][B(C_6F_5)_4]$ (*9.2* mg, *0.01* mmol) was then added through a syringe under vigorous stirring. The polymerization was quenched after 5 minutes by adding methanol (*150* mL) [1].

References Cited (or Bibliography)

[1] H. Wang, Y. Yang, M. Nishiura, Y. Higaki, A. Takahara, and Z. Hou, "Synthesis of Self-Healing Polymers by Scandium-Catalyzed Copolymerization of Ethylene and Anisylpropylenes," *J. Am. Chem. Soc.*, 2019, doi: 10.1021/jacs.8b13316.

[2] J. Móczó and B. Pukánszky, "Polymer micro and nanocomposites: Structure, interactions, properties," *J. Ind. Eng. Chem.*, vol. 14, no. 5, pp. 535–563, Sep. 2008, doi: 10.1016/j.jiec.2008.06.011.

[3] L. S. Nair and C. T. Laurencin, "Biodegradable polymers as biomaterials," *Prog. Polym. Sci. Oxf.*, vol. 32, no. 8–9, pp. 762–798, Aug. 2007, doi: 10.1016/j.progpolymsci.2007.05.017.

[4] V. Guarino, G. Gentile, L. Sorrentino, and L. Ambrosio, "Polycaprolactone: Synthesis, Properties, and Applications," in *Encyclopedia of Polymer Science and Technology*, John Wiley & Sons, Inc., 2017, pp. 1–36. doi: 10.1002/0471440264.pst658.

[5] P. Grossen, D. Witzigmann, S. Sieber, and J. Huwyler, "PEG-PCL-based nanomedicines: A biodegradable drug delivery system and its application," *J. Controlled Release*, vol. 260, pp. 46–60, Aug. 2017, doi: 10.1016/j.jconrel.2017.05.028.

[6] C. Chiari *et al.*, "A tissue engineering approach to meniscus regeneration in a sheep model," *Osteoarthritis Cartilage*, vol. 14, no. 10, pp. 1056–1065, Oct. 2006, doi: 10.1016/j.joca.2006.04.007.

[7] P. Gunatillake, R. Mayadunne, and R. Adhikari, "Recent developments in biodegradable synthetic polymers," *Biotechnol. Annu. Rev.*, vol. 12, pp. 301–347, 2006, doi: 10.1016/S1387-2656(06)12009-8.

[8] J. Zhu, W. Cao, M. Yue, Y. Hou, J. Han, and M. Yang, "Strong and stiff aramid nanofiber/carbon nanotube nanocomposites," *ACS Nano*, vol. 9, no. 3, pp. 2489–2501, Mar. 2015, doi: 10.1021/nn504927e.

[9] Z. Liu, J. Lyu, D. Fang, and X. Zhang, "Nanofibrous Kevlar Aerogel Threads for Thermal Insulation in Harsh Environments," *ACS Nano*, vol. 13, no. 5, pp. 5703–5711, May 2019, doi: 10.1021/acsnano.9b01094.

[10] A. Patel *et al.*, "High Modulus, Thermally Stable, and Self-Extinguishing Aramid Nanofiber Separators," *ACS Appl. Mater. Interfaces*, vol. 12, no. 23, pp. 25756–25766, Jun. 2020, doi: 10.1021/acsami.0c03671.

[11] V. M. Fonseca, E. J. P. A. Oliveira, P. T. Lima, and L. H. Carvalho, "DEVELOPMENT OF KEVLAR COMPOSITES FOR BALLISTIC APPLICATION," ABEC Publicacoes, Jul. 2018, pp. 548–553. doi: 10.21452/bccm4.2018.09.04.

[12] T. J. Singh and S. Samanta, "Characterization of Kevlar Fiber and Its Composites: A Review," in *Materials Today: Proceedings*, Elsevier Ltd, 2015, pp. 1381–1387. doi: 10.1016/j.matpr.2015.07.057.

[13] J. M. Koo *et al.*, "Nonstop Monomer-to-Aramid Nanofiber Synthesis with Remarkable Reinforcement Ability," *Macromolecules*, vol. 52, no. 3, pp. 923–934, Feb. 2019, doi: 10.1021/acs.macromol.8b02391.

[14] B. Yang, L. Wang, M. Zhang, J. Luo, and X. Ding, "Timesaving, High-Efficiency Approaches to Fabricate Aramid Nanofibers," *ACS Nano*, vol. 13, no. 7, pp. 7886–7897, Jul. 2019, doi: 10.1021/acsnano.9b02258.

[15] M. Yang *et al.*, "Dispersions of aramid nanofibers: A new nanoscale building block," *ACS Nano*, vol. 5, no. 9, pp. 6945–6954, Sep. 2011, doi: 10.1021/nn2014003.

[16] X. He, Y. Qu, J. Peng, T. Peng, and Z. Qian, “A novel botryoidal aramid fiber reinforcement of a PMMA resin for a restorative biomaterial,” *Biomater. Sci.*, vol. 5, no. 4, pp. 808–816, Apr. 2017, doi: 10.1039/c6bm00939e.

[17] N. Kobayashi, H. Izumi, and Y. Morimoto, “Review of toxicity studies of carbon nanotubes,” *J. Occup. Health*, vol. 59, no. 5, pp. 394–407, 2017, doi: 10.1539/joh.17-0089-RA.

[18] L. Horváth, A. Magrez, B. Schwaller, and L. Forró, “Toxicity Study of Nanofibers,” in *Supramolecular Structure and Function 10*, Springer Netherlands, 2011, pp. 133–149. doi: 10.1007/978-94-007-0893-8_9.

[19] B. A. Patterson, M. H. Malakooti, J. Lin, A. Okorom, and H. A. Sodano, “Aramid nanofibers for multiscale fiber reinforcement of polymer composites,” *Compos. Sci. Technol.*, vol. 161, pp. 92–99, Jun. 2018, doi: 10.1016/j.compscitech.2018.04.005.

[20] M. A. Woodruff and D. W. Hutmacher, “The return of a forgotten polymer - Polycaprolactone in the 21st century,” *Prog. Polym. Sci. Oxf.*, vol. 35, no. 10, pp. 1217–1256, 2010, doi: 10.1016/j.progpolymsci.2010.04.002.

[21] N. Noroozi, J. A. Thomson, N. Noroozi, L. L. Schafer, and S. G. Hatzikiriakos, “Viscoelastic behaviour and flow instabilities of biodegradable poly (ε-caprolactone) polyesters,” *Rheol. Acta*, vol. 51, no. 2, pp. 179–192, Feb. 2012, doi: 10.1007/s00397-011-0586-6.

[22] C. S. Miranda, A. R. M. Ribeiro, N. C. Homem, and H. P. Felgueiras, “Spun biotextiles in tissue engineering and biomolecules delivery systems,” *Antibiotics*, vol. 9, no. 4, Apr. 2020, doi: 10.3390/antibiotics9040174.

[23] Y. Fan, Z. Li, and J. Wei, “Application of aramid nanofibers in nanocomposites: A brief review,” *Polymers*, vol. 13, no. 18, Sep. 2021, doi: 10.3390/polym13183071.

[24] G. M. Odegard, T. S. Gates, K. E. Wise, C. Park, and E. J. Siochi, “Constitutive modeling of nanotube-reinforced polymer composites,” *Compos. Sci. Technol.*, vol. 63, no. 11, pp. 1671–1687, 2003, doi: 10.1016/S0266-3538(03)00063-0.

[25] J. Lin, S. H. Bang, M. H. Malakooti, and H. A. Sodano, “Isolation of Aramid Nanofibers for High Strength and Toughness Polymer Nanocomposites,” *ACS Appl. Mater. Interfaces*, vol. 9, no. 12, pp. 11167–11175, Mar. 2017, doi: 10.1021/acsami.7b01488.

[26] A. Campopiano, A. Cannizzaro, A. Olori, and S. Boccanera, “STUDY OF A SELECTION OF MAN-MADE ORGANIC FIBRES.”

[27] “Standard Test Method for Tensile Properties of Plastics 1”, doi: 10.1520/D0638-14.

[28] S. J. Nelson, J. J. Creechley, M. E. Wale, and T. J. Lujan, “Print-A-Punch: A 3D printed device to cut dumbbell-shaped specimens from soft tissue for tensile testing,” *J. Biomech.*, vol. 112, Nov. 2020, doi: 10.1016/j.jbiomech.2020.110011.

[29] “Standard Test Method for Compressive Properties of Rigid Plastics 1”, doi: 10.1520/D0695-15.

[30] “Standard Test Method for Shear Strength of Plastics by Punch Tool 1”, doi: 10.1520/D0732-17.

[31] E. Kim and H. Changani, “Study of dynamic mechanical behavior of aluminum 7075-T6 with respect to diameters and L/D ratios using Split Hopkinson Pressure Bar (SHPB),” *Struct. Eng. Mech.*, vol. 55, no. 4, pp. 857–869, Aug. 2015, doi: 10.12989/sem.2015.55.4.857.

[32] B. A. G. Schrauwen, L. C. A. V. Breemen, A. B. Spoelstra, L. E. Govaert, G. W. M. Peters, and H. E. H. Meijer, “Structure, deformation, and failure of flow-oriented semicrystalline

polymers,” *Macromolecules*, vol. 37, no. 23, pp. 8618–8633, Nov. 2004, doi: 10.1021/ma048884k.

[33] C. Sorini, A. Chattopadhyay, and R. K. Goldberg, “Micromechanical modeling of the effects of adiabatic heating on the high strain rate deformation of polymer matrix composites,” *Compos. Struct.*, vol. 215, pp. 377–384, May 2019, doi: 10.1016/j.compstruct.2019.02.016.

Appendix A: The Complete SHPB Stress Strain Rate Graphs

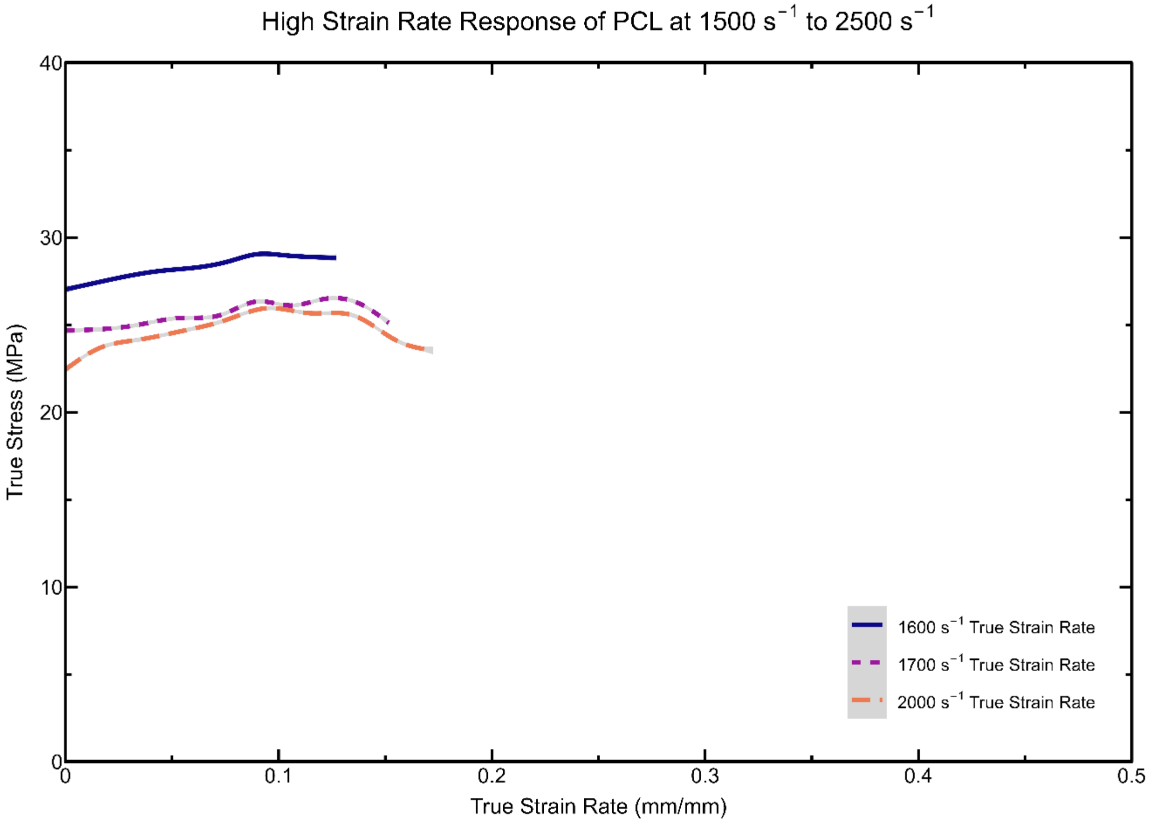
High Strain Rate Response of PCL at 1500 s^{-1} to 2500 s^{-1}

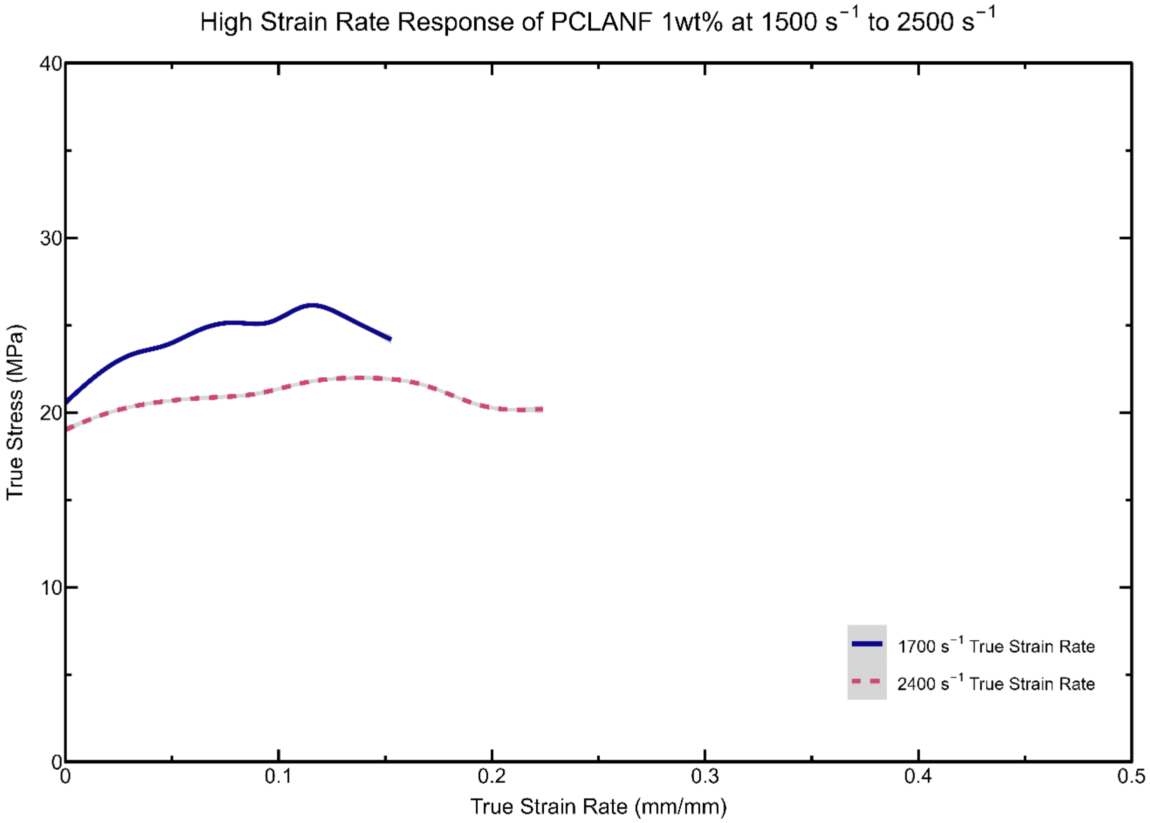
High Strain Rate Response of PCLANF 1wt% at 1500 s^{-1} to 2500 s^{-1}

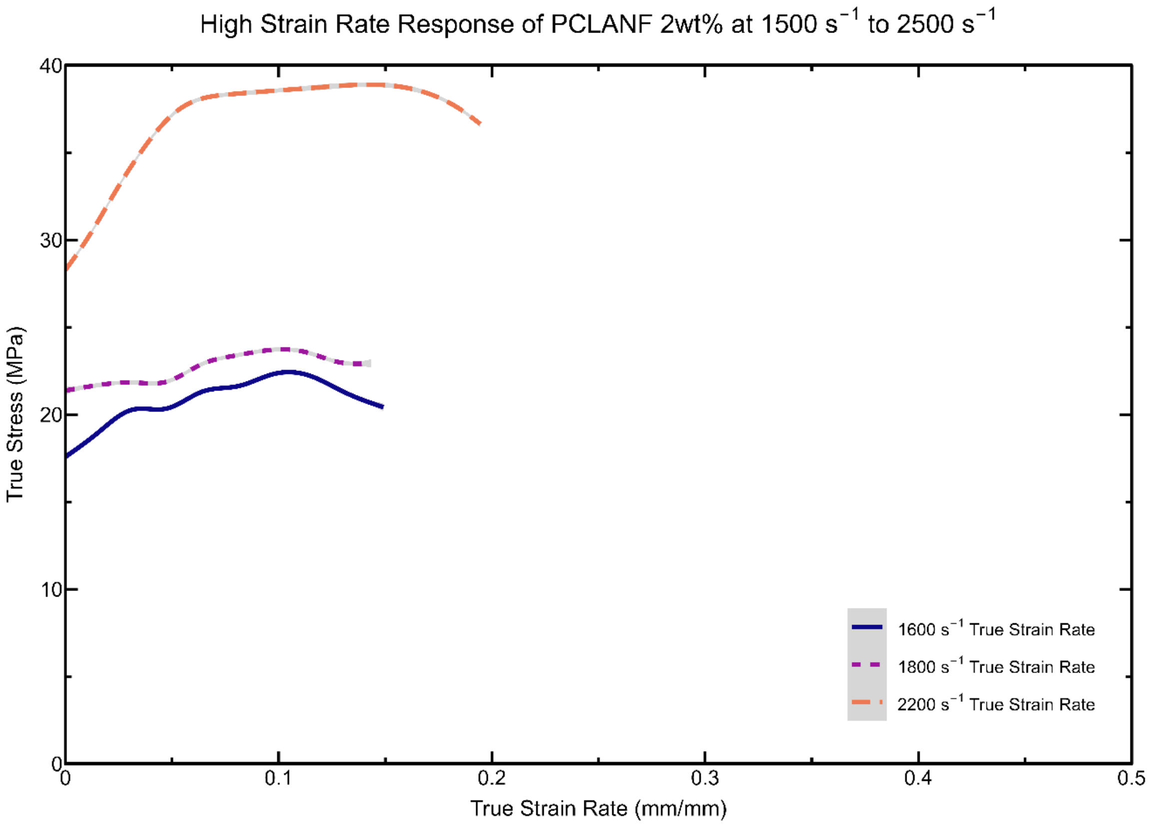
High Strain Rate Response of PCLANF 2wt% at 1500 s^{-1} to 2500 s^{-1}
True Stress (MPa)
0
10
20
30
40
True Strain Rate (mm/mm)
0
0.1
0.2
0.3
0.4
0.5
1600 s^{-1} True Strain Rate
1800 s^{-1} True Strain Rate
2200 s^{-1} True Strain Rate

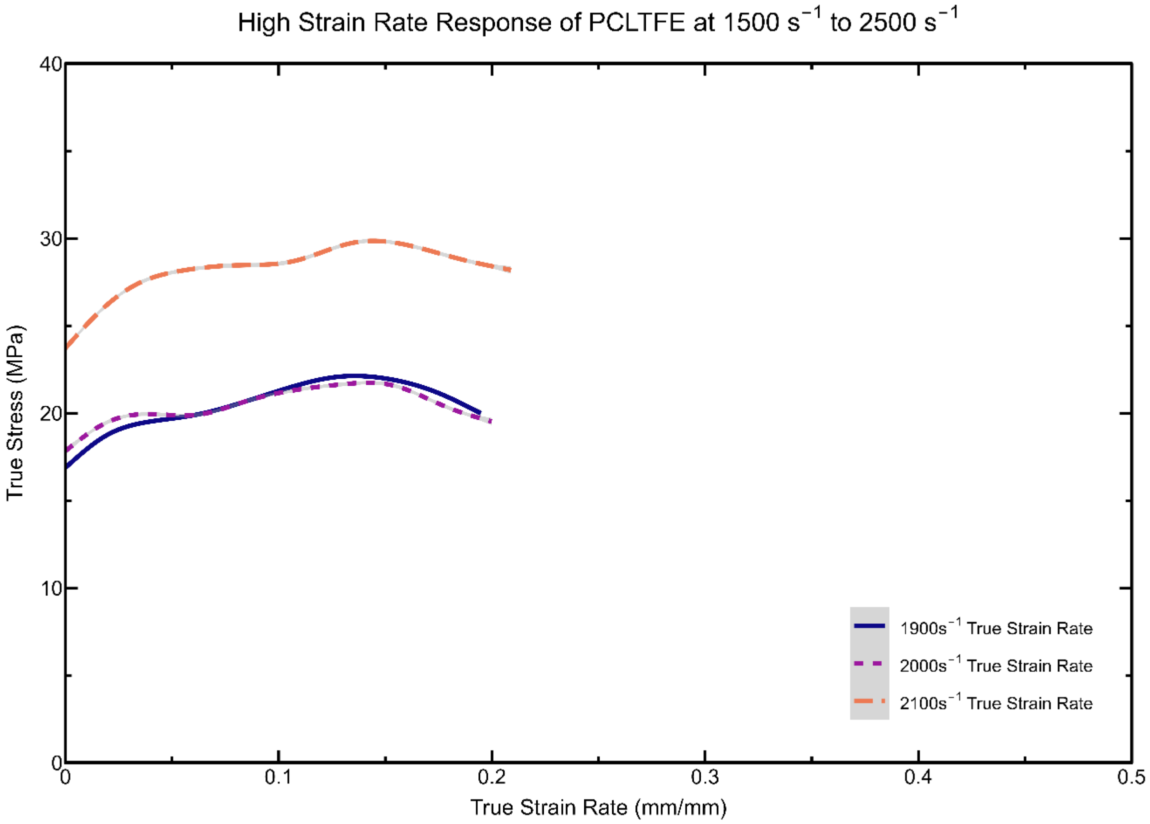
High Strain Rate Response of PCLTFE at 1500 s^{-1} to 2500 s^{-1}
True Stress (MPa)
0
10
20
30
40
True Strain Rate (mm/mm)
0
0.1
0.2
0.3
0.4
0.5
1900s^{-1} True Strain Rate
2000s^{-1} True Strain Rate
2100s^{-1} True Strain Rate

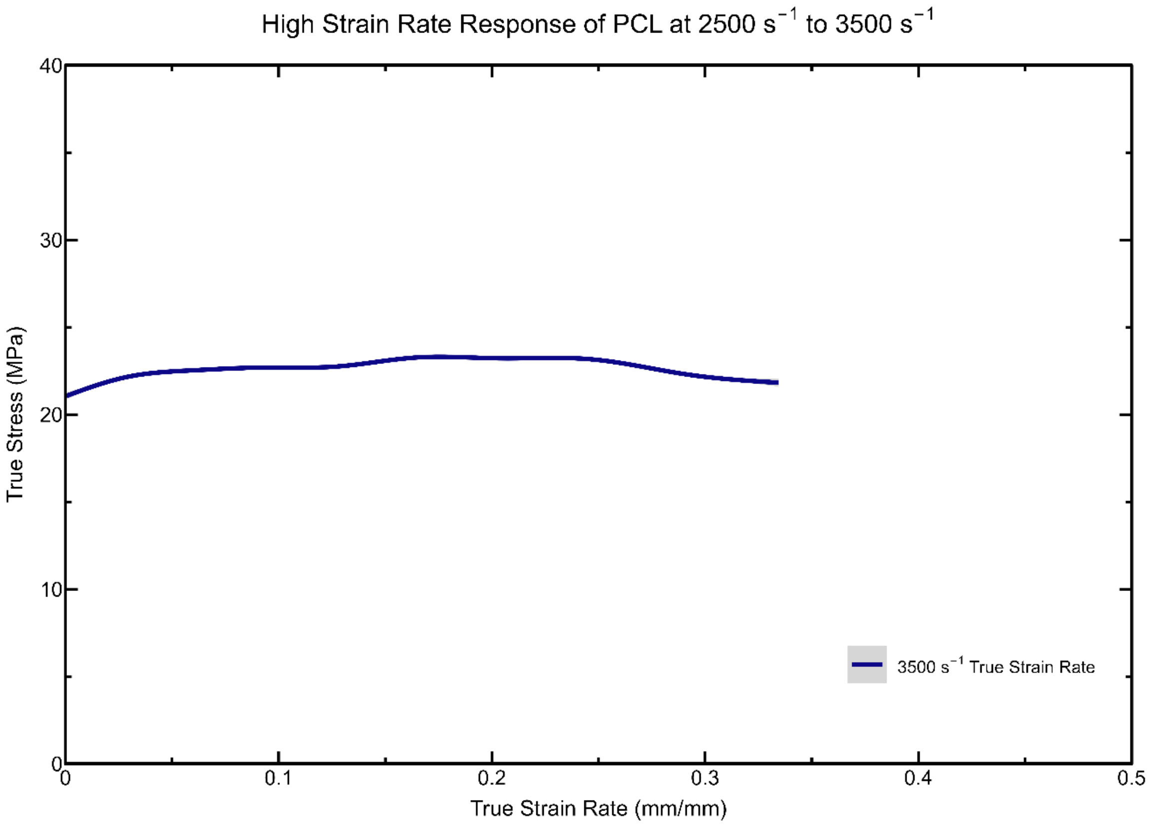
High Strain Rate Response of PCL at 2500 s^{-1} to 3500 s^{-1}
True Stress (MPa)
0
10
20
30
40
True Strain Rate (mm/mm)
0
0.1
0.2
0.3
0.4
0.5
3500 s^{-1} True Strain Rate

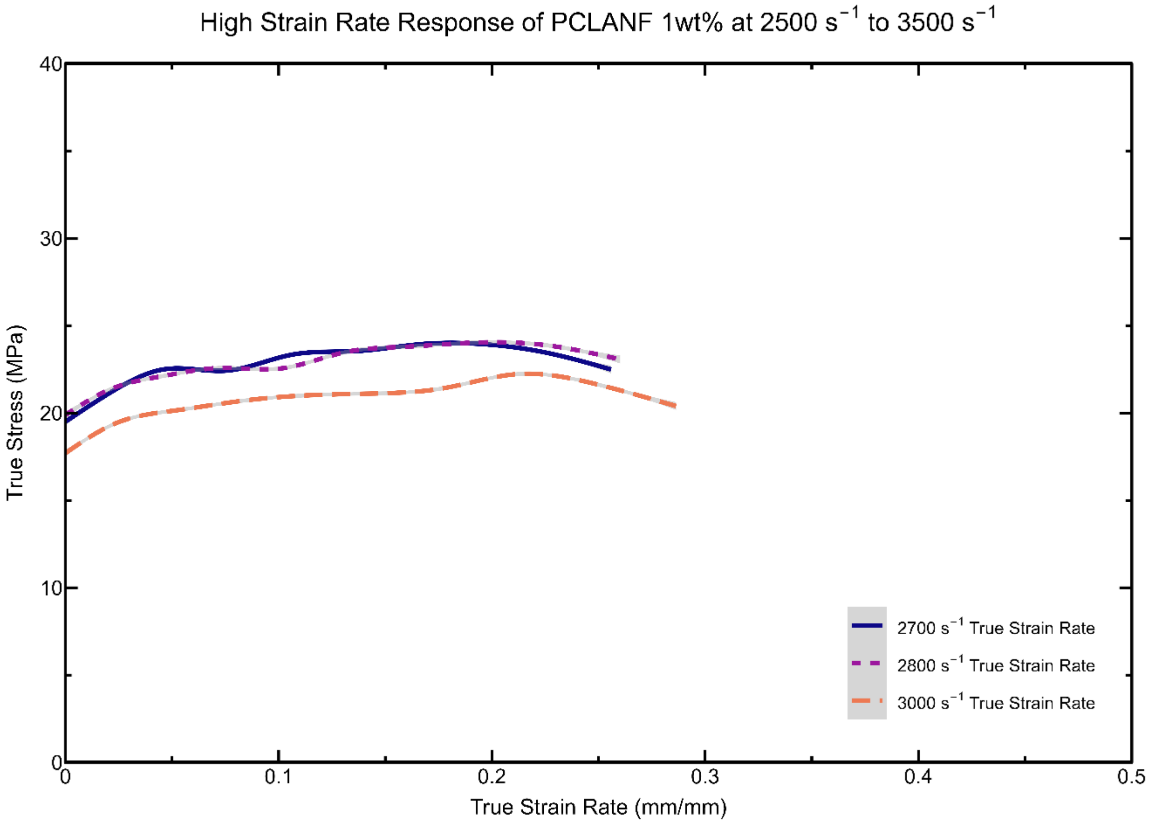
High Strain Rate Response of PCLANF 1wt% at 2500 s^{-1} to 3500 s^{-1}
True Stress (MPa)
0
10
20
30
40
True Strain Rate (mm/mm)
0
0.1
0.2
0.3
0.4
0.5
2700 s^{-1} True Strain Rate
2800 s^{-1} True Strain Rate
3000 s^{-1} True Strain Rate

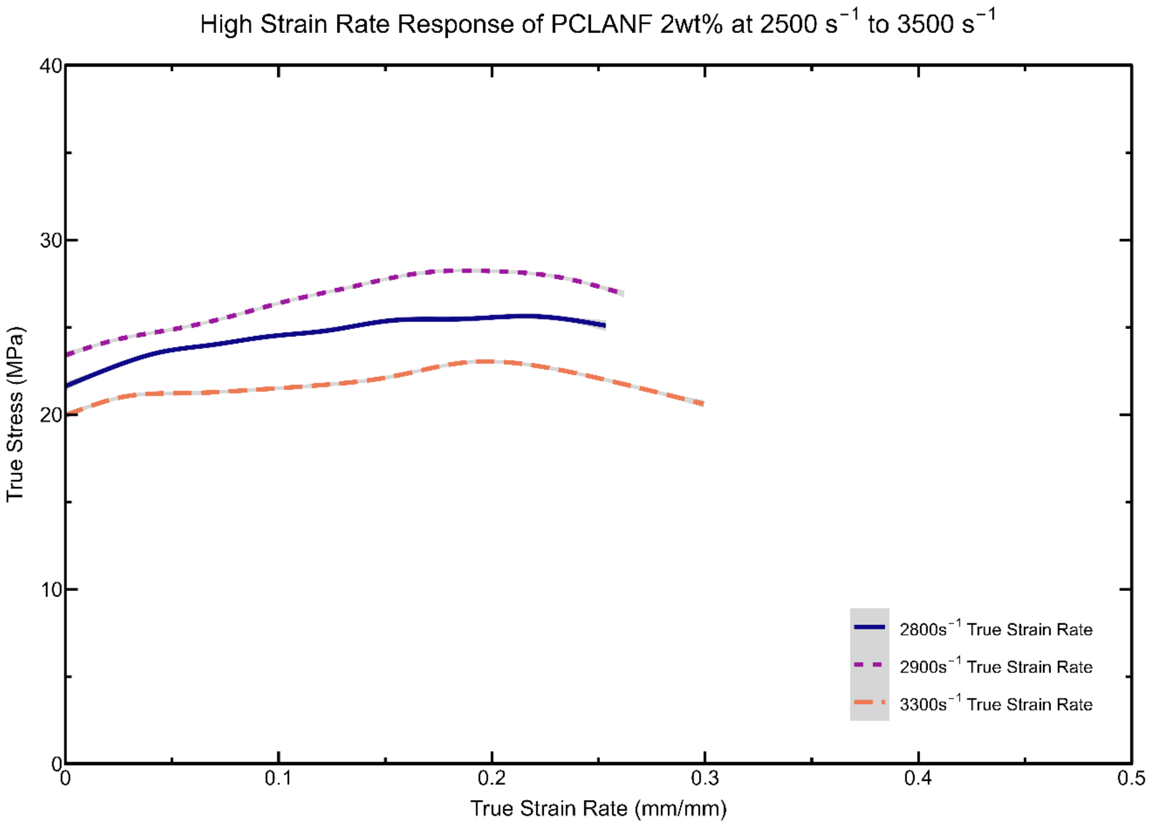
High Strain Rate Response of PCLANF 2wt% at 2500 s^{-1} to 3500 s^{-1}
True Stress (MPa)
True Strain Rate (mm/mm)
0
10
20
30
40
0.1
0.2
0.3
0.4
0.5
2800s^{-1} True Strain Rate
2900s^{-1} True Strain Rate
3300s^{-1} True Strain Rate

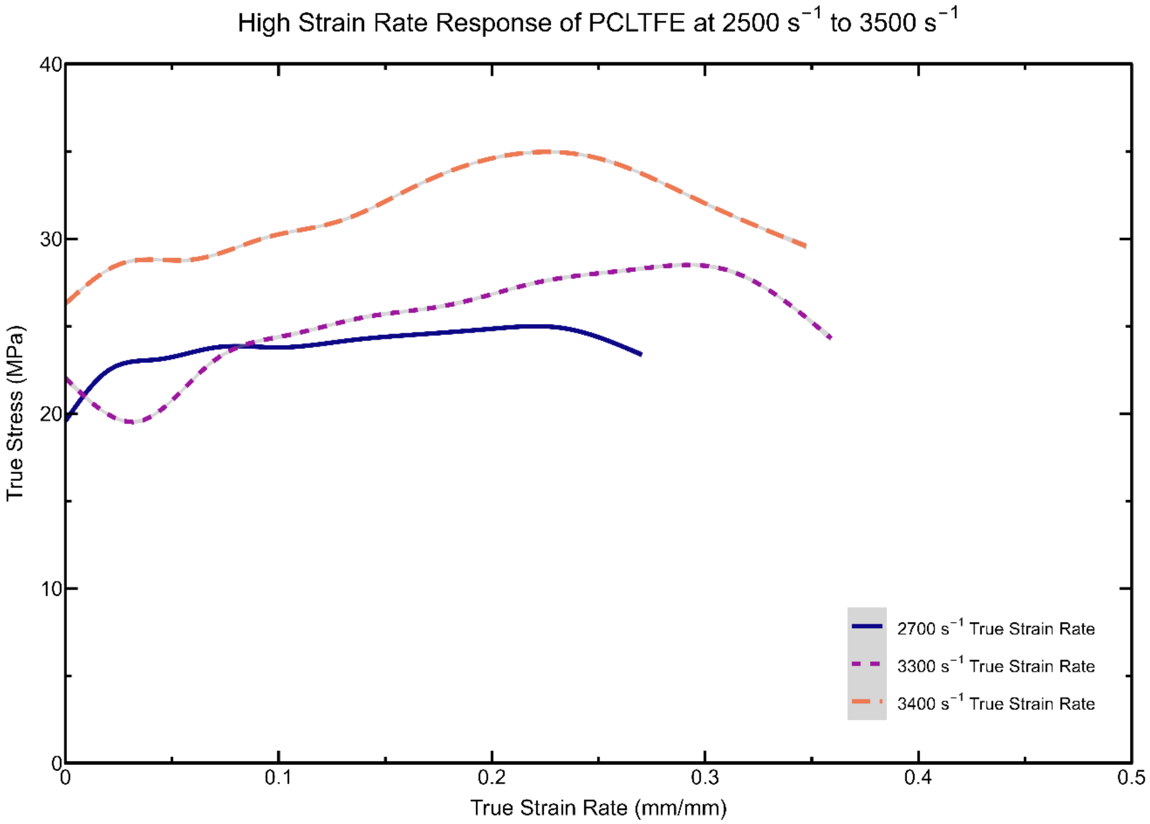
High Strain Rate Response of PCLTFE at 2500 s^{-1} to 3500 s^{-1}
True Stress (MPa)
True Strain Rate (mm/mm)
0
10
20
30
40
0.1
0.2
0.3
0.4
0.5
2700 s^{-1} True Strain Rate
3300 s^{-1} True Strain Rate
3400 s^{-1} True Strain Rate

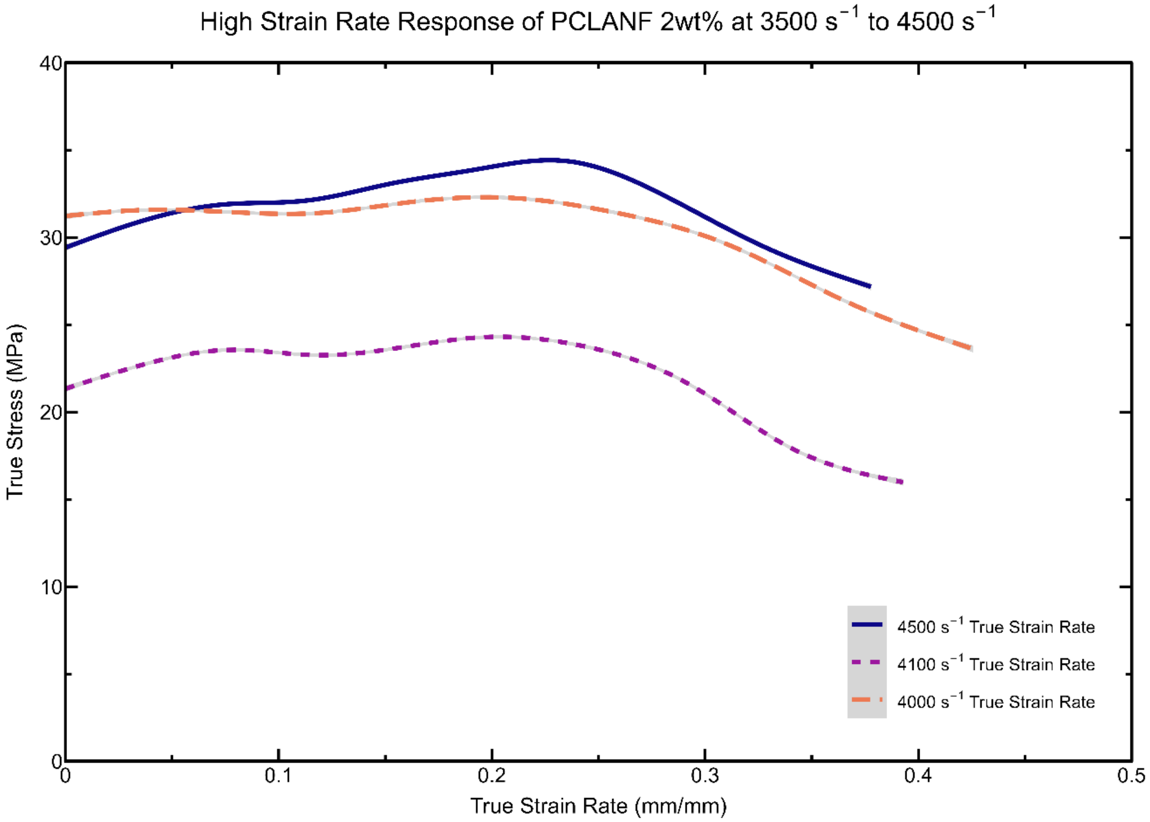
High Strain Rate Response of PCLANF 2wt% at 3500 s^{-1} to 4500 s^{-1}
True Stress (MPa)
0
10
20
30
40
True Strain Rate (mm/mm)
0
0.1
0.2
0.3
0.4
0.5
4500 s^{-1} True Strain Rate
4100 s^{-1} True Strain Rate
4000 s^{-1} True Strain Rate

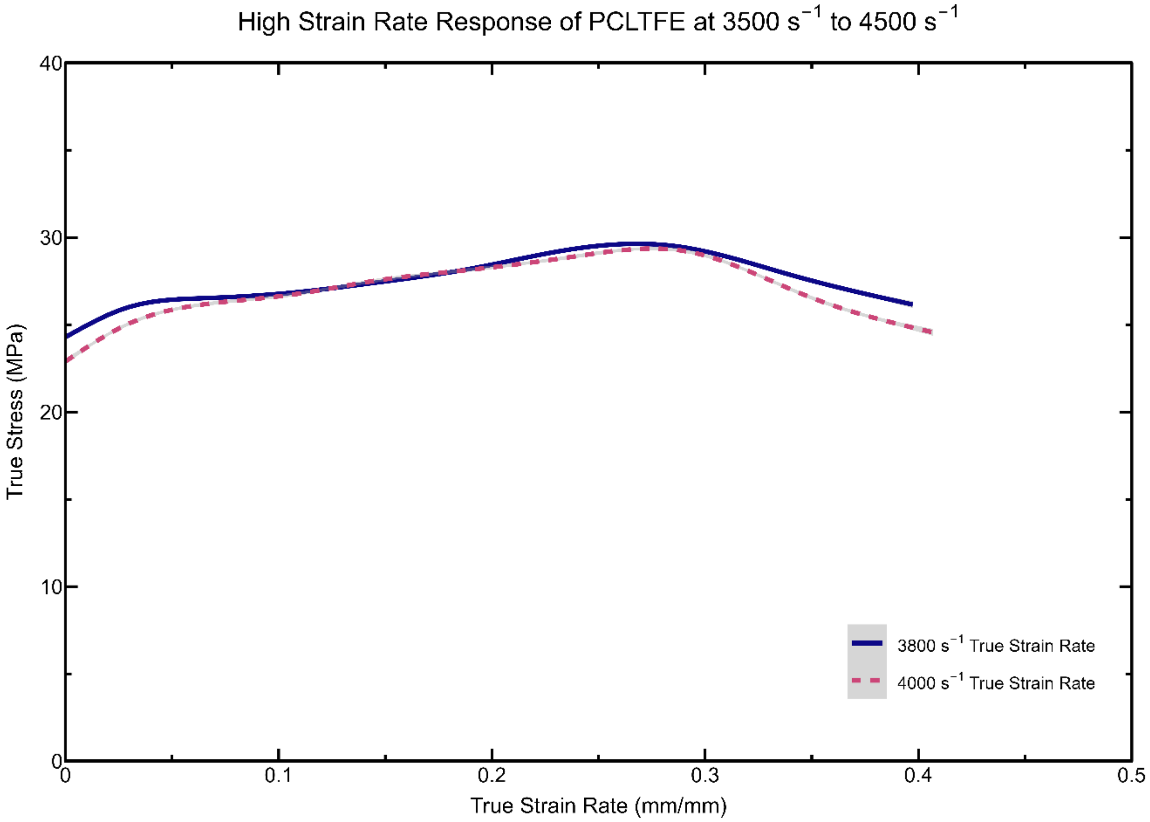
High Strain Rate Response of PCLTFE at 3500 s^{-1} to 4500 s^{-1}
True Stress (MPa)
0
10
20
30
40
True Strain Rate (mm/mm)
0
0.1
0.2
0.3
0.4
0.5
3800 s^{-1} True Strain Rate
4000 s^{-1} True Strain Rate